Relative importance of conceptual and computational errors when delineating saltwater intrusion from resistivity inverse models in heterogeneous coastal aquifers

Andrés González-Quirós[a*], Jean-Christophe Comte[a]

[a]School of Geosciences, University of Aberdeen, Aberdeen, UK

*Corresponding author: andres.quiros@abdn.ac.uk | Tel. +44 (0)12 2427 2321

Andrés González-Quirós (ORCID ID: 0000-0003-1102-8626)

Jean-Christophe Comte (ORCID ID: 0000-0002-5129-8391)

Highlights:

- Inverted resistivity data are commonly used to delineate saltwater intrusion (SWI).
- Errors associated to inversion and petrophysical transformation are assessed.
- A coupled modelling approach was applied to four synthetic heterogeneous aquifers.
- Inversion and salinity recovery errors are equivalent when neglecting heterogeneity.
- Spatial quantification of the errors is key for geophysics-aided SWI management.

Abstract

In coastal areas, geological heterogeneity influences the geometry and characteristics of the freshwater-saltwater mixing zone. Geophysical electrical and electromagnetic methods are increasingly used to delineate the freshwater-saltwater mixing zone or for groundwater model calibration. However, in practical applications, it is common when assessing pore water salinity from resistivity models to disregard the spatial variability of the aquifer properties assuming pore salinity is the dominant control on bulk electrical conductivity. In this paper we use a coupled hydrogeophysical model to assess the discrepancies in recovered salinity caused by the geophysical inversion and the application of the chosen petrophysical model when heterogeneity is ignored. We find that errors made when neglecting heterogeneity during petrophysical transformation are equivalent or higher in magnitude than inversion errors, more so when an inappropriate petrophysical model is used, but exhibit different spatial distribution. The results show that their combined effect results in significant overestimation of the spreading of the mixing zone. The analysis provides new insights to the groundwater community to better evaluate the reliability of geophysically-derived information when delineating the freshwater-saltwater interface or when geophysics is used quantitatively as part of model scenario simulation, uncertainty analysis or optimisation strategies.

Keywords: *Coastal aquifers, Heterogeneity, Electrical resistivity, Petrophysical model, Hydrogeophysics.*

1 Introduction

Coastal aquifers are important and strategic water resources under increasing pressure (Jiao and Post, 2019). Fresh groundwater in coastal environments are in a dynamic equilibrium with seawater. Over-abstraction may lead to seawater intrusion (SWI) into abstraction wells,

which then become saline and unsuitable for purposes such as for drinking and irrigation (Werner et al., 2013). To avoid this, an appropriate management of coastal aquifers is crucial and requires a good understanding of the dynamics of the saltwater interface.

Geological heterogeneity, and associated spatial variations of aquifer properties, is common in natural environments (Koltermann and Gorelick, 1996) and exert a major control on the spatio-temporal dynamics of saltwater in coastal aquifers. Over the recent years, several studies have analysed the impact of heterogeneity on the patterns of the freshwater-saltwater mixing zone. This includes theoretical, synthetic modelling and/or laboratory sandbox experiments which have evaluated the combined effect of heterogeneity with tidal oscillations (Pool et al., 2015), the influence of common discrete features such as fringing reefs or dykes (Houben et al., 2018) or the presence of connected higher permeability materials that lead to preferential flowpaths in large-scale seawater circulation (Michael et al., 2016). All concluded that heterogeneity plays a fundamental role on saltwater intrusion, generally leading to an increase in the spreading of the mixing zone (Kerrou and Renard, 2010), which is higher in low conductivity layers in stratified aquifers (Lu et al., 2013). Heterogeneity also influences the geometry and inland penetration of the mixing zone (Pool et al., 2015; Michael et al., 2016) increasing the risk of salinization of pumping wells (Yu and Michael, 2019).

Because of the difficulties to characterize real systems, especially with small-scale heterogeneities, most previous works based on synthetic modelling approaches have introduced heterogeneities in the simulation using various techniques that range from conceptual zonation — for example for the evaluation of multilayered or stratified aquifers (Lu et al., 2013) or common discrete structures such as dykes or fringing reefs (Houben et al., 2018) — to geostatistical approaches — using sequential Gaussian simulation (SGS) (Kerrou and Renard, 2010; Pool et al., 2015, Siena and Riva., 2018) or sequential indicator simulation (SIS) (Michael et al., 2016; Yu and Michael, 2019).

In real-world (in situ) studies, heterogeneity identification relies on the analysis of sharp differences in groundwater levels (Marshall et al., 2020), tidal attenuation analysis (Rotzoll et al., 2013), geophysical interpretation (Kirkegaard et al., 2011), in the inversion of groundwater models (Michael and Voss, 2009; Kerrou et al., 2013) or a combination of these (e.g. Comte et al., 2017).

In in-situ studies, the hydrogeological characterization of the subsurface, including the delineation of both structural heterogeneities and the mixing zone between freshwater and saltwater requires the collection of high spatial resolution, and therefore large, datasets and/or computationally expensive numerical models. Enough spatial coverage is usually not achievable from direct borehole observations which often do not have the high density required to capture the spatial variability (heterogeneity) of aquifer properties and hydrologic variables (e.g. Binley et al., 2010).

Geophysical non-invasive techniques are increasingly used to provide indirect sampling of the subsurface at high spatiotemporal resolution (Binley et al., 2015). Electrical and electromagnetic methods, in particular, are popular in coastal hydrogeological studies because they are highly sensitive to pore water salinity (Wilson et al., 2006), which allows for spatio-temporal delineation of the freshwater-saltwater mixing zone. Geophysical information can be used at multiple stages in groundwater studies. In the literature it is possible to find several examples that range from qualitative interpretation approaches, in in which the geophysical data are processed and interpreted independently from groundwater data or models, and further used as part of the conceptualisation of the hydrogeological system (e.g. De Franco et al., 2009), to more integrative and quantitative approaches, in which geophysics is used to parameterise, calibrate and/or verify groundwater models. While the qualitative approach is relatively common in coastal aquifer studies (Jiao and Post, 2019), the more accurate

89 quantitative approach is less documented and the focus of more recent research efforts (Comte
90 and Banton, 2007; Nguyen et al., 2009; Beaujean et al., 2014; Comte et al., 2017).

91 In the last decade, the potential of using geophysics as additional data sets for the
92 calibration of groundwater models has led to an increase of interest in the development of joint
93 or coupled hydrogeophysical modelling and inversion strategies (Ferré et al., 2009; Steklova
94 and Haber, 2017), where both geophysical and groundwater data are modelled together. This
95 requires the transformation of hydrogeological variables and properties of interest into
96 geophysical signals (and vice versa) by using appropriate petrophysical relationships (e.g.
97 Archie, 1942 when using geo-electrical or electromagnetic methods). These petrophysical
98 models, however, are often applied with the assumption that petrophysical parameters are
99 constant in space (i.e. homogeneity). When using geoelectrical methods, the observed
100 geophysical response is influenced not only by saltwater distribution in the aquifer, but also by
101 petrophysical heterogeneity (e.g. Brunetti et al., 2017), which contradicts the common
102 assumption taken in coastal studies that electrical resistivity variations are solely related to
103 saltwater concentration variations. It is also common to select a single petrophysical model
104 when dealing with variable lithology, even when it is known that some relationships are more
105 appropriate for a specific geological media. For example, Archie's law, which applies to clay-
106 free porous media, has been and is still widely applied in clayey materials, which has led to
107 incorrect interpretations (Revil et al., 2017). As a result, an inappropriate application of these
108 petrophysical relationships for the parametrization or calibration of groundwater models could
109 be an important source of error, which adds up to the errors resulting from the inversion of
110 geophysical data, including typical smoothing of sharp subsurface structures and loss of
111 sensitivity with distance to the geophysical source (e.g. Linde, 2014).

112 In this paper we aim to assess or identify the possible sources of error when determining
113 salinity concentrations from electrical resistivity data. Our overall objective is to evaluate the

cumulated effect of geological heterogeneities, the petrophysical model and the ERI inversion on the recovered distribution of salinities. To perform the study, we use a coupled multiphysics modelling methodology to evaluate the saltwater distribution in a set of heterogeneous hydrogeological scenarios and the simulated response obtained by an electrical resistivity survey. Our objective is to identify and illustrate the sources of error and their potential implications for reliable interpretation of geophysical data in real-world coastal aquifers. It is important for the groundwater scientist and practitioner to better differentiate between accurate and less accurate/unreliable information contained in geophysically-derived salinity patterns. Such assessment is needed to provide a degree of confidence when delineating the location and geometry of the freshwater-saltwater interface, and further interpret this into risk and/or timescale of salinization for water wells or ecosystems receptors, or more quantitatively, use it as part of groundwater model scenario simulation or optimisation. The results show that sources of errors add-up and lead to inaccuracies in the estimated spreading and position of the seawater-freshwater mixing zone. This has important implication for the calibration of groundwater models with geophysically-derived salinity and shows the usefulness of coupled modelling methodologies and accurate hydrogeological conceptualization in hydrogeophysical studies.

2 Problem Statement

The relationship between freshwater and denser seawater in a coastal aquifer is not a sharp interface as observed between two immiscible liquids, a conceptualization used sometimes to simplify calculations, such as in the well-known Ghyben-Herzberg approximation. Instead, this relationship is a mixing zone between high and low concentration of dissolved salts, implying high and low fluid density; that is, a concentration/density gradient (**Fig. 1**). This mixing zone, also referred to as transition zone (e.g. Bear and Cheng, 2010) has

138 a variable width which is controlled by the groundwater system hydrodynamics, influenced by
139 its boundary conditions (freshwater recharge, pumping, tides, etc.) and by the spatial
140 distribution of aquifer hydraulic properties associated to the subsurface geology. As a result,
141 the morphology of the salt/freshwater transition zone can be spatially (3D) and temporally very
142 complex and its thickness highly variable, from centimetres to kilometres (e.g. Jiao and Post,
143 2019).

144 It is common to use additional geophysical techniques to indirectly identify and
145 characterize the seawater-freshwater interface and the distribution of hydraulic properties in
146 the subsurface, in order to complement discrete and scattered direct measurement from
147 boreholes. Electromagnetics (EM) in a broad sense (including direct current DC resistivity and
148 transient EM) are popular geophysical techniques extensively used in many applications. They
149 provide information of the distribution of subsurface electrical resistivity/conductivity that can
150 be linked to geological properties and state variables. These geophysical techniques are well
151 suited to investigate coastal aquifers as subsurface electrical conductivity strongly increases
152 with pore water salinity. EM surveys conducted on the ground surface or in a borehole are
153 therefore able to detect saltwater as an increase in electrical conductivity.

154 The relationship between pore water salinity and bulk electrical conductivity has been
155 described by petrophysical relationships (Lesmes and Friedman, 2005). These relationships,
156 however, relate bulk electrical conductivity, to not only the fluid conductivity and saturation,
157 but also values and distributions of physical properties of the porous/fractured media, referred
158 to as petrophysical parameters, which are spatially variable in real world heterogeneous aquifer
159 systems. The most widely used petrophysical relationship in this context, Archie's law (Archie,
160 1942), requires information on the porosity, cementation and tortuosity of the porous medium.

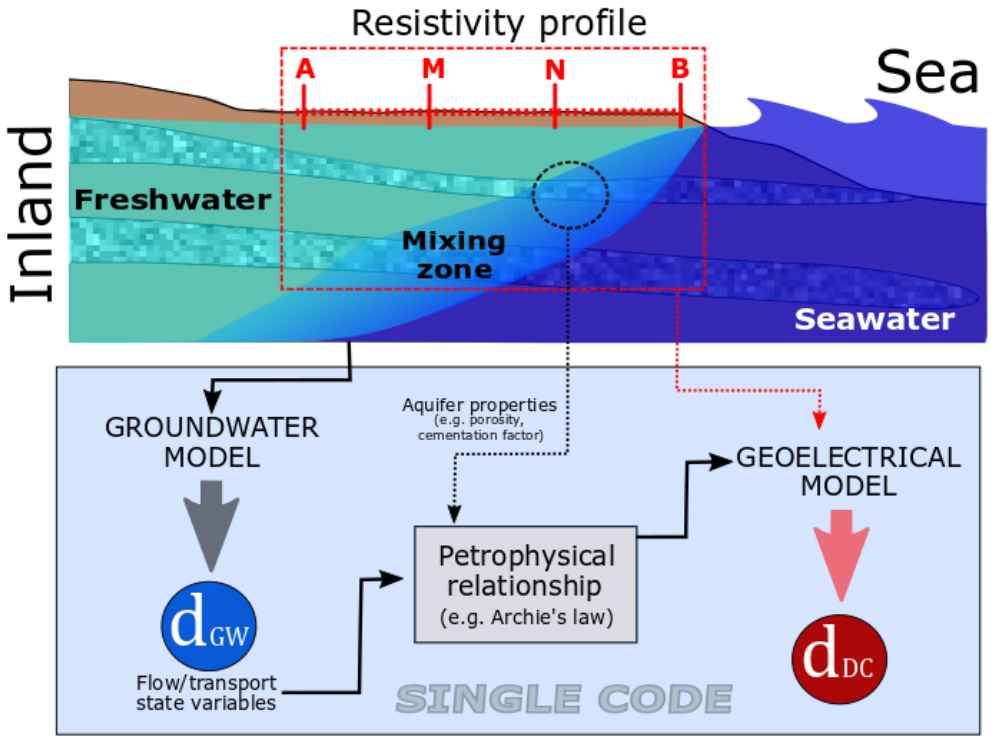

161

162 ***Fig. 1. Up)*** *Schematic representation of the geophysical monitoring of a seawater intrusion problem in*
163 *a heterogeneous aquifer.* ***Down:*** *Flowchart of the numerical coupling procedure. GW for groundwater*
164 *model and DC for the electrical model.*

165 In order to produce the most realistic geophysical response of the combined effect of
166 geological heterogeneous properties and hydrological state variables, we aim to solve in a
167 single code the three linked mathematical problems, that is, the groundwater, petrophysical and
168 geophysical models. In this paper we use the geoelectrical (DC resistivity) response taken as
169 an illustrative example (**Fig. 1**). First, the variable-density SWI groundwater model solves the
170 two coupled non-linear equations for flow and transport providing pore water salinity
171 distribution. Then, the petrophysical model is computed using, as input, spatially variable water
172 electrical conductivities calculated from water salinities and petrophysical parameters. Finally,
173 the geoelectrical model is solved for field conditions of data acquisition on the ground surface.

3 Materials and Methods

3.1 General methodology

The next sections explain the coupled modelling methodological approach used to explore the influence of heterogeneity in geoelectrical (DC resistivity) monitoring of coastal aquifers. In section 3.2 and 3.3 we outline the procedure applied to solve the groundwater and geoelectrical problems in COMSOL Multiphysics. In section 3.4 we describe the equations and petrophysical models that link both problems and explain how the coupled hydrogeoelectrical model is solved. Finally, we explain how electrical resistivities are recovered from forward electrical model after inversion (3.5).

The same general hydrogeophysical procedure is applied to four synthetic hydrogeological settings: a homogeneous model (CASE#0) and three geologically heterogeneous models (identified as cases #1, #2 and #3). All four scenarios have the same model domain, boundary conditions and electrical survey characteristics.

3.2 Saltwater Intrusion Models

3.2.1 General characteristics and homogeneous model (CASE#0)

The seawater intrusion model was performed in 2D as a vertical slice perpendicular to the coast using a modification of the standard conditions of the well-known Henry's problem (Henry, 1964). The aquifer was defined as confined, homogeneous and with constant thickness, b, except on the seaside dipping boundary where thickness decreases. A fixed, depth-varying, seawater pressure (Dirichlet) boundary condition was applied on the seaside face. A constant freshwater influx (Neumann boundary condition) was imposed on the inland face. Salt mass

fractions, ω [-], of 1 (salt concentrations in total dissolved solids, TDS, of 35 g l^{-1} or kg m^{-3}) and 0, were applied at the sea and upstream boundaries, respectively (**Fig. 2**).

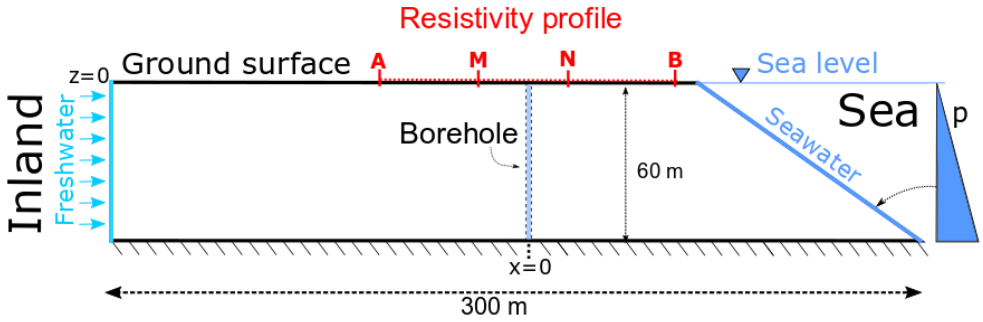

Fig. 2. *Schematic characteristics of the hydrogeological model used as base scenario.*

The SWI model was solved through the following coupled governing equations for steady-state variable density groundwater flow —mass conservation (1) and Darcy's law (2)— and non-reactive transport (3) (e.g. Bear and Cheng, 2010)

$$\nabla(\rho \boldsymbol{q}) = 0, \tag{1}$$

$$\boldsymbol{q} = -\frac{k}{\mu}(\nabla p + \rho g \nabla z), \tag{2}$$

$$\frac{\partial(\phi \rho C)}{\partial t} + \nabla(\rho C \boldsymbol{q}) - \nabla(\rho \boldsymbol{D} \nabla C) = 0. \tag{3}$$

In the equations above, $\boldsymbol{q}$ is the specific discharge [L T^{-1}]; p [M L^{-1} T^{-2}] is pressure; g is gravity acceleration (assumed constant 9.8 m s^{-2}); z [L] elevation; ϕ [-] porosity; k [L^2] is the intrinsic permeability; ρ [M L^{-3}] and μ [M L^{-1} T^{-1}] fluid density and viscosity. C [M L^{-3}] is the solute concentration, which here is equal to the normalized salt mass fraction, ω [-], and takes values between 0 and 1 as explained above. D [L^2 T^{-1}] is the dispersion coefficient. Both balance equations were coupled using the following expression that links salt concentration with water density

$$\rho = \rho_0 \left(1 + \beta \frac{C}{C_s}\right), \quad (4)$$

209 ρ_0, is the reference density (density of freshwater), C_s is the normalized concentration of
210 seawater (here 1) and β is the density difference factor (Zhou et al, 2005).

211 These equations were solved in COMSOL Multiphysics for the domain and parameters
212 presented in **Fig. 2** and **Table 1**.

213 ***Table 1.*** *Henry's model parameters. See Fig. 2 for interpretation.*

Parameter	Symbol	Value	Unit
Aquifer length	x	300	m
Aquifer thickness	b	60	m
Saltwater density	ρ_s	1025	kg m^{-3}
Freshwater density	ρ_0	1000	kg m^{-3}
Saltwater salinity	TDS	35	g l^{-1}
Freshwater electrical conductivity	σ_{Fw}	500	µS cm^{-1}
Saltwater electrical conductivity	σ_{Sw}	50000	µS cm^{-1}
Hydraulic conductivity	K_h	1×10^{-5}	m s^{-1}
Effective porosity	ϕ	0.33	-
Molecular diffusion	D_m	1×10^{-9}	m^2 s^{-1}
Longitudinal dispersivity	α_L	5	m
Transversal dispersivity	α_T	0.5	m
Inland freshwater inlet	q_{in}	1.5×10^{-3}	m d^{-1}

214 ### 3.2.2 Heterogeneous models

215 The homogeneous model was further amended to produce three heterogeneous scenarios
216 aiming to study the effect of geological heterogeneity on the freshwater-seawater mixing zone,
217 the petrophysical model and the imaging capabilities of electrical resistivity imaging. The
218 models presented cover a selection of available strategies for generating realistic
219 heterogeneities: a vertical dyke (**CASE#1**) with hydrogeological properties assigned with
220 zonation; and two models created using geostatistical approaches: sequential indicator
221 simulation (**CASE#2**) and sequential Gaussian simulation (**CASE#3**).

222 ***CASE#1: Dyke Model***

223 The first model (**CASE#1**) represents a costal aquifer where the saltwater intrusion
224 extension is restricted by the existence of a narrow vertical low permeability formation, e.g. a
225 volcanic dyke (**Fig. 3**). This model was based on the general conceptualisation from a recent
226 synthetic study conducted by Houben et al (2018). In this scenario, the dyke acted as a low
227 permeability vertical barrier hosted in a more permeable rock, a sandstone. The model
228 properties and boundary conditions, aside from the hydraulic properties of the dyke itself which
229 are based on estimations from Comte et al. (2017), were identical to these presented in the
230 homogeneous case. Material properties used for the non-dyke domain were those of the
231 reference sand used in the homogeneous model. Other specific characteristics and properties
232 used in CASE#1 model are compiled in **Table 2**.

233 ***Table 2.*** *Main characteristics of the dyke model CA.*

Parameter	Symbol	Value	Unit
Depth to dyke top	D_D	10	m
Dyke thickness	T_D	2	m
Distance from coastline to dyke	L_D	35	m
Sandstone			
Hydraulic Conductivity	K_S	1×10^{-5}	m s^{-1}
Longitudinal dispersivity	α_L	5	m
Transversal dispersivity	α_T	0.5	m
Dyke			
Hydraulic Conductivity	K_D	2.8×10^{-8}	m s^{-1}
Porosity	ϕ_D	0.01	-
Longitudinal dispersivity	α_L	0.5	m
Transversal dispersivity	α_T	0.05	m

234 ***CASE#2: Sequential Indicator Simulation Model***

235 An alternative methodology uses geostatistical techniques for the incorporation of
236 heterogeneities. In this paper we applied two (unconditional) geostatistical simulation
237 techniques for the simulation of property fields.

The first proposed example (**CASE#2**) used sequential indicator simulation (SIS) (e.g. Journel, 1989). This technique can be used for the generation of categorical variables, such as facies distributions, and has been used recently in hydrogeological studies to evaluate the influence of heterogeneity in seawater circulation and saltwater patterns in the continental shelf and pumping induced SWI (Michael et al., 2016; Yu and Michael, 2019). In this illustrative example we used the code ISIM3D (Gomez-Hernandez and Srivastava, 1990) to simulate 4 different facies (categorical property fields) compiled in **Table 3**. The resulting spatial distribution is shown in #2 in **Fig. 3**.

Table 3. *Property values for the four facies used to simulate the SIS scenario CASE#2.*

Facies	ID	Hydraulic Cond. (m/s)
Coarse Sand	1	10^{-4}
Medium sand	2	10^{-5}
Shaly sand	3	10^{-6}
Clay	4	10^{-11}

CASE#3: Sequential Gaussian Simulation Model

In the second geostatistical approach (**CASE#3**) we used a sequential Gaussian simulation (SGS) technique, which has been previously applied in some SWI studies, both theoretical (Kerrou and Renard, 2010; Pool et al., 2015) and in real-world applications (Kerrou et al., 2013; Siena and Riva, 2018). Isotropic, unconditional, log permeability fields, $Y(x) = \ln k(x)$, were simulated using the software GCOSIM3D (Gomez-Hernandez and Journel, 1993) with mean $\langle Y \rangle = \ln k_M$, $\sigma_Y^2 = 1$ and a correlation scale $\lambda = 50\, m$ (see hydraulic conductivity distribution in #3 in **Fig. 3**).

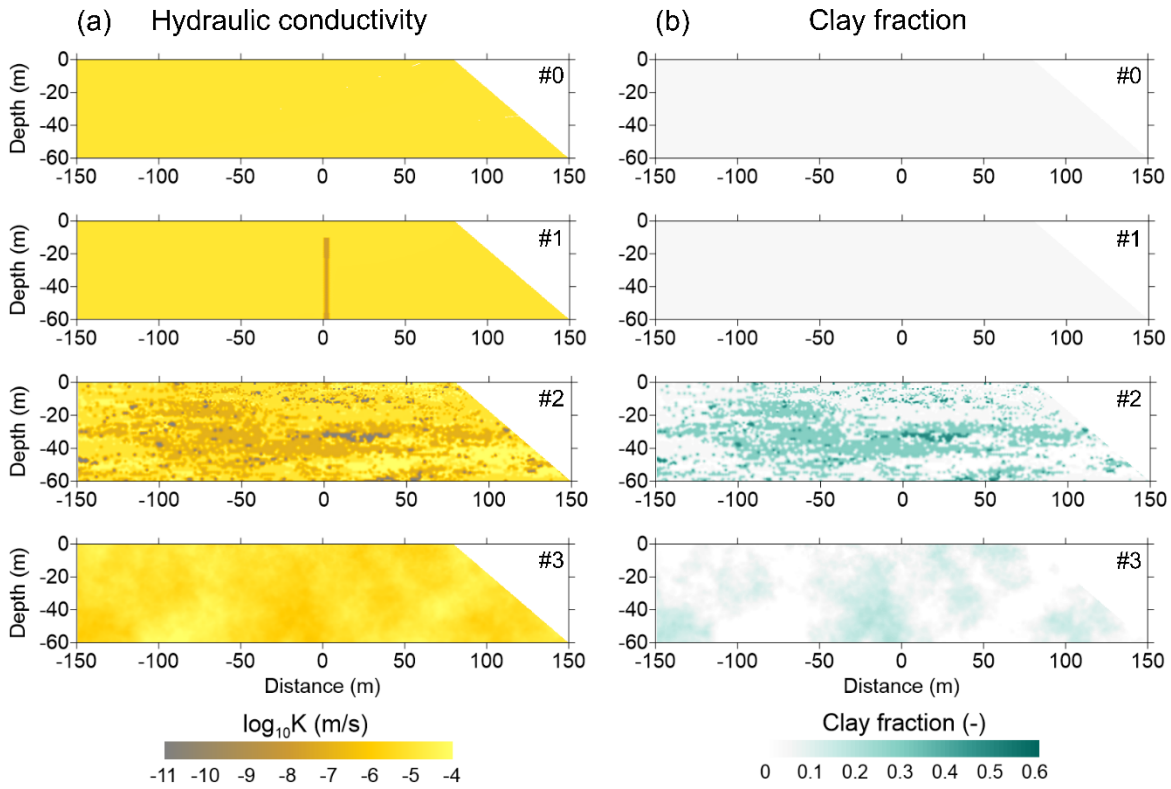

255

256 ***Fig. 3.*** *Distribution of hydraulic conductivity* ***(a)*** *and clay fraction* ***(b)*** *for the four modelled scenarios*
257 *#0-3. The equations used to assign clay content are explained in detail in section 3.4.*

258 ## 3.3 DC Resistivity Model

259 The virtual DC electrical resistivity acquisition for all the models was performed on a
260 line of 72 electrodes perpendicular to the coastline with 2 m spacing centred at coordinate $x =$
261 0 (**Fig. 2**) using a Wenner-alpha array.

262 The governing equation of the electrical problem for calculation of the electrical potential
263 caused by a point source, I [A], on a three-dimensional domain under steady state conditions
264 is expressed as

$$-\nabla \cdot [\sigma(x,y,z)\nabla U(x,y,z)] = I\delta(x-x_0)\delta(y-y_0)\delta(z-z_0), \quad (5)$$

σ is the electric conductivity (in S·m^{-1}), U [V] is the electric potential and δ is the Dirac delta. Note that resistivity (in Ohm·m or Ω·m) is $1/\sigma$.

On the ground surface was imposed a zero current (Neumann) boundary condition, $\frac{\partial U}{\partial \boldsymbol{n}} = 0$ and in the external boundary the following mixed boundary condition applied $\frac{\partial U}{\partial n} + \frac{\cos\theta}{r} U = 0$ where r is the distance from the measuring point to the source and θ the angle between r and the outward normal direction to the boundary, n.

For a 3D model, the equations above can be easily implemented in COMSOL Multiphysics® (Butler and Singha, 2014). However, to solve the electrical problem in the proposed 2D domain, we must assumed symmetry in the y direction (perpendicular to the studied section); that is, the distribution of electrical conductivity in the subsurface is $\sigma(x, z)$. To retain the 3D point sources (this problem is sometimes referred to as 2.5D modelling) the problem was solved in the Fourier domain (Dey and Morrison, 1979). After Fourier cosine transform, the following equation is obtained

$$-\nabla \cdot [\sigma(x,z)\nabla \bar{U}(x,\omega,z)] + k^2\sigma(x,z)\bar{U}(x,k,z) = \frac{I}{2}\delta(x-x_0)\delta(z-z_0). \quad (6)$$

This equation was solved in a two-dimensional domain (x, z) for selected wavenumbers (k) in COMSOL (González-Quirós et al., 2019). The use of a limited optimized number of wavenumbers (5 in this work) allowed to achieve a reasonable accurate solution while minimising the computational effort (Xu et al., 2000). Additionally, the mixed boundary condition was substituted by a Dirichlet boundary condition (Blome et al., 2009). This required the model domain to be kept large enough, which was achieved using infinite elements in order to avoid the subsequent increment in computational cost.

A parametric sweep was used to compute pole-pole potentials for each of the modelled electrodes and all the wavenumbers. In this case, the solution of the electrical resistivity model

in 2.5D required to solve a total of $N_{electrodes} \times N_{wavenumbers}$ model runs. The electrical potentials, $\bar{U}$, computed in the 2.5D Fourier domain were back-transformed to a 3D Cartesian domain by the inverse Fourier cosine transform, where g_i is a weighting coefficient

$$U(x,y,z) = \frac{2}{\pi}\int_0^\infty \bar{U}(x,z,k)\cos(ky)\,dk \approx \sum_{i=1}^{n} \bar{U}(x,z,k)\,g_i. \quad (7)$$

Finally, the superposition principle was used to calculate the desired 4-point electrode of the Wenner-alpha array (**Fig. 1**).

3.4 Coupled Hydrogeoelectrical Models

3.4.1 Conversion from fluid salinity to fluid electrical conductivity

The solution of the coupled hydrogeophysical model required the solution of both models, hydrogeological and geophysical, linked by an appropriate transfer function, the petrophysical relationship. This function transforms the relevant hydrogeological parameters and state variables into bulk electrical conductivities.

To calculate bulk electrical conductivities, σ_b, first, the salinity concentrations calculated in the groundwater model were converted to water electrical conductivities, σ_w. This conversion encompassed two steps. First, salt mass fractions, ω [-] (see section 3.2.1) were transformed into total dissolved solids (TDS). Later, TDS ($mg \cdot l^{-1}$) were converted into fluid electrical conductivities, σ_w ($\mu S \cdot cm^{-1}$). The following linear conversion equation between fluid electrical conductivity and TDS was used (Jiao and Post, 2019)

$$TDS = k_c\,\sigma_w. \quad (8)$$

The conversion factor k_c changes with the chemical composition of water but typical values range between 0.55 and 0.75 (Hem, 1985). In this work we chose a value of $k_c = 0.7$

obtained by using the relationship $k_c = TDS_{SW}/\sigma_{Sw}$ (Jiao and Post, 2019) where TDS_{SW}=35000 mg l^{-1} (35 kg·m^{-3}) and σ_{Sw}=50000 µS·cm^{-1} (5 S·m^{-1}) are, respectively, the total dissolved solids and fluid electrical conductivities for seawater used in the numerical model (**Table 1**).

3.4.2 Petrophysical relationship

Once the fluid electrical conductivity was obtained, the bulk electrical conductivity of the saturated porous media was computed by application of a petrophysical relationship. Here, we used the Waxman and Smits (1968) relationship to simulate the bulk conductivity in the subsurface. Unlike Archie's model, Waxman and Smits accounts for the electrical properties of clay minerals and is therefore appropriate for facies where clay is present (e.g. Revil et al., 1998)

$$\sigma_{bulk} = \frac{1}{F}(\sigma_w + BQ_v), \quad (9)$$

σ_w is fluid conductivity [S m^{-1}] and F is the formation factor, ($F = 1/\phi^m$), where ϕ is the porosity and m [-] is the cementation exponent. The value of m can range between 1 and 5 (e.g. Glover, 2009), typically 1.5-2.5 for sandstones and above 2.5, up to 5, for carbonates (Cai et al., 2017). B is the equivalent counterion mobility, $B = B_0\left[1 - 0.6e^{(-\sigma_w/0.013)}\right]$, where B_0 = 4.78×10^{-8} is the maximum counterion mobility. Q_v [meq·ml^{-1}] is the excess of surface charge per unit pore volume calculated as (Revil et al., 1998)

$$Q_v = \rho_g\left(\frac{1-\phi}{\phi}\right)CEC. \quad (10)$$

CEC [meq·g^{-1}] is the cation exchange capacity. The value of *CEC* is proportional to clay content and depends on the nature of the clay minerals (Revil et al., 1998). An appropriate

expression (Patchett, 1975) such as $CEC = \varphi_w^{cl} \times 0.08$ was used here. 0.08 is a CEC_i value in meq·g^{-1}.

The Waxman and Smits' petrophysical relationship was applied to the facies defined as containing a certain amount of clay (e.g. Power et al., 2013). Where the sandstone materials are clay free, the Waxman and Smits equation reduces to Archie's law (Archie, 1942)

$$\sigma_{bulk} = \frac{1}{F}\sigma_w. \tag{11}$$

A threshold was used to define the lower permeability value of clay-free sands beyond which clay was present, using the expression (Revil and Cathles, 1999)

$$k_{sd} = \frac{d_{sd}^2(\phi_{sd})^{3m_{sd}}}{24}, \tag{12}$$

d_{sd}^2 is the grain diameter of sand, ϕ_{sd} the sand porosity and m_{sd} is the sand cementation exponent. Values are assigned in this work according to Power et al. (2013): $d_{sd}^2 = 2 \times 10^{-4}$ m, $\phi_{sd} = 0.32$ and $m_{sd} = 2$. In this work we used $m_{sd} = \mathrm{m_{cs}} = 2$ (Kang et al., 2019).

Equation (12) was used to compute the volumetric clay content, clv, for those materials with permeability lower than the clay-free sand threshold (Revil and Cathles, 1999)

$$\begin{cases} k < k_{sd} & clv = \dfrac{k_{sd}^{\frac{1}{3m_{cs}}} - k^{\frac{1}{3m_{cs}}}}{k_{sd}^{\frac{1}{3m_{cs}}}\left(\dfrac{1-\phi_{cl}}{\phi_{sd}}\right)} \\ k > k_{sd} & clv = 0 \end{cases} \tag{13}$$

Total porosity was computed from the following expression (Berg, 1995)

$$\phi = \phi_{sd}(1 - clv) + \phi_{cl}\, clv. \quad (14)$$

339 Finally, mass fractions of clay and sand grains, φ_w^{cl} and φ_w^{sd} respectively, were computed
340 using the following equations (Power et al., 2013; Kang et al., 2019)

$$\varphi_w^{cl} = \frac{\mathrm{clv}(1-\phi_{cl})\rho_{cl}}{\mathrm{clv}(1-\phi_{cl})\rho_{cl}+(1-clv)(1-\phi_{sd})\rho_{sd}}, \quad (15)$$

$$\varphi_w^{sd} = 1 - \varphi_w^{cl}. \quad (16)$$

341 Density of mineral grains was assumed the same for sand and clay particles, $\rho_{cl} = \rho_{sd} =$
342 $\rho_g = 2650$ kg·m^{-3}. Constant temperature of 25 ºC was assumed in the study. Clay fraction
343 distributions for the studied scenarios after application of these equations are shown in **Fig. 3**.

344 ***Table 4.*** *Parameters of the petrophysical model.*

Parameter	Symbol	Value	Unit	Reference
Grain diameter of sand	d_{sd}^2	2×10^{-4}	m	Power et al. (2013)
Porosity of sand	ϕ_{sd}	0.32	-	Power et al. (2013)
Sand cementation exponent	m_{sd}	2	-	Kang et al. (2019)
Clay-free permeability threshold	k_{sd}	3.55×10^{-12}	m^2	Power et al. (2013)
Porosity of clay	ϕ_{cl}	0.47	-	Mesri and Olson (1971)
Clayey sand cementation exponent	m_{cs}	2	-	Revil et al. (1998)
Grain density	ρ_g	2650	kg m^{-3}	

345 ## 3.5 ERI inversion

346 For the ERI inversion the simulated forward electrical responses (quadrupoles of
347 Wenner-alpha arrays of 72 electrodes) from the four modelled scenarios were contaminated
348 with 3% uncorrelated Gaussian noise (e.g., Nussbaumer et al., 2019). The inversion was
349 performed with the code BERT (Boundless Electrical Resistivity Tomography) (Günther and

Rücker, 2019), which solves electrical resistivity forward (Rücker et al., 2006) and inverse (Günther et al., 2006) problems using the finite element method implemented in unstructured meshes. BERT uses a smoothness-constrained, Occam's type, inversion (Constable et al., 1987), with minimisation of the objective function using a Gauss-Newton approach (Günther et al., 2006). The objective function is a combination of a weighted data misfit term, ϕ_d, and a model roughness term, ϕ_m, weighted by using a regularization parameter, λ,

$$\phi = \phi_d + \lambda\phi_m = \left\|D\left(d - f(m)\right)\right\|_2^2 + \lambda\|C(m - m^0)\|. \quad (17)$$

$d - f(m)$ are the data residuals between measured (here synthetic noised) data, d, and the forward electrical response, $f(m)$, of model m. D is a matrix that contains the inverse of measurement errors. C is a regularization weighting matrix to keep the model, m, close to a reference model, m^0.

The same mesh was used for all models. The regularisation parameter (λ) was chosen using the L-curve criterion (Günther et al., 2006). No anisotropy and an estimated relative error model of 3% were assumed. The inversion stopped when data fitted within the error levels (chi-squared criterion) such as $\chi^2 = \phi_d/N \approx 1$, where N is the number of data (828 for the Wenner-alpha array in this study).

4 Results

4.1 Forward coupled model results

The forward coupled hydroelectrical model was solved in steady-state conditions in less than 2 min on a computer desktop with processor Intel® Core™ i5-8500 with 40 GB RAM for the single groundwater and the 360 (72 electrodes × 5 wavenumbers) electrical model runs. After solving both problems, a geoelectrical forward response of the system was obtained

without requirements for intermediate post-processing or data conversions. The benefit of including the petrophysical relationship in the way presented here is that it honours the spatial variability of geological parameters.

In this section we present the results of the forward hydrogeological model, that is, the salinity distribution and the resulting bulk resistivities, obtained for the four scenarios.

Fig. 4a shows the salinity distribution obtained after solving the groundwater model. In all result sections three reference TDS (or total dissolved solids) iso-contours of 1, 17.675 (0.5 salt-mass fraction) and 34.65 kg·m^{-3} (0.99 salt-mass fraction) are represented to show the spreading of the freshwater-seawater mixing zone. The iso-contour $TDS = 1$ kg·m^{-3} (black line) will be thereafter termed drinking water limit (DWL). The DWL contour is used to delineate a reference position of the upper salinity limit for drinkable freshwater. We have also defined three descriptors to characterize the SWI. A characteristic width of the mixing zone (W_{MZ}), is measured in the bottom of the aquifer between the 0.25 and 0.75 salt mass fraction iso-concentration contours. Additionally, two descriptors for SWI penetration were defined as a reference toe penetration (P_{Toe}), measured between the coastline ($x = 80$ m) and the 0.5 iso-concentration contour (ω = 0.5, red line) at the bottom of the aquifer, and DWL tip penetration (P'_{DWL}), measured between the coastline and the DWL at the top of the aquifer. P_{Toe} and P'_{DWL} are illustrated in the CASE#0 model results section in **Fig. 4a**.

Fig. 4b shows the calculated (thereafter referred as 'true') bulk resistivities after application of Waxman and Smits petrophysical relationship honouring the true spatial (hydrogeological) variability, that is, both heterogeneous petrophysical parameters and fluid electrical conductivity. For evaluation we analysed the computed maximum and minimum model resistivities. For identification of the saltwater-freshwater mixing zone we present the results of resistivities computed along the DWL (black line) and 0.5 (red line) salt mass fraction iso-contours. The results are compiled in **Table 5**.

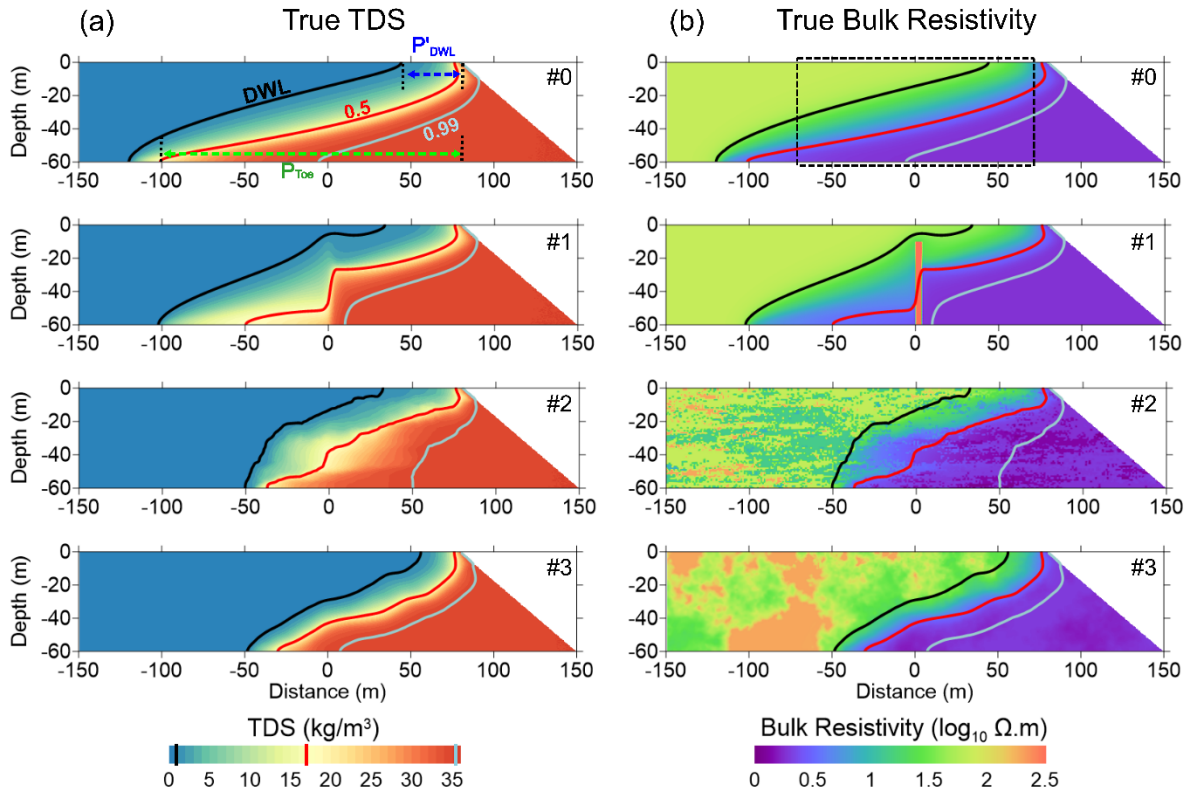

Fig. 4. *Results of the forward model. TDS* ***(a)*** *and bulk resistivity* ***(b)****. Contour lines in both models are for TDS reference values corresponding to the DWL (black) and salt mass fractions of 0.5 (red) and 0.99 (light blue). In section* ***a#0****, there are illustrated the metrics* P_{Toe} *and* P'_{DWL} *used to describe the salinity distribution and the saltwater-freshwater mixing zone. Dashed box in* ***b#0*** *represents the domain of investigation of the resistivity section shown in the following figures.*

The homogeneous scenario (#0 in **Fig. 4**) showed a smooth transition of salinity values across the mixing zone. Computed minimum and maximum bulk resistivity (Res_{Min} and Res_{Max}) ranged between 1.8 Ω·m in the pure saltwater region (bottom right of the section) and 70.2 Ω·m in the freshwater zone (top left). Bulk resistivity values obtained along the DWL and the higher salinity (0.99) contours, were Res_{DWL} = 40.9 Ω·m and Res_{sw} = 1.85 Ω·m, respectively.

In the dyke scenario (#1), the vertical structure acts as a low permeability barrier to the seawater encroachment. This pattern is observed in **Fig. 4** with reference TDS contour lines exhibiting a step shape. Computed W_{MZ} = 89.7 m, reflects the widening of the mixing zone because of the existence of the dyke. The dyke led to shorter toe penetration than in the homogeneous scenario. The computed resistivities were different in the two geological

412 domains: in the sandstone domain, extreme values were the same computed in the
413 homogeneous (sandstone) scenario (**Table 5**); in the dyke, however, minimum and maximum
414 bulk resistivities were much higher in the bottom (saltwater) and top (low salinity but not
415 drinkable water) regions of the dyke, respectively. These higher values result from the very
416 low porosity assigned to the dyke domain. Resistivities for the reference TDS contours in the
417 sandstone were equal to those of scenario #0 except within the dyke, where for the central 0.5
418 TDS (red) contour computed resistivity was 2506 Ω·m, three orders of magnitude higher than
419 for the same contour in the sandstone domain (3.5 Ω·m).

420 In the heterogeneous scenarios the distribution of hydraulic properties caused spatial
421 variability in the width of the mixing zone. In model #2, the salinity distribution was strongly
422 controlled by the heterogeneity of hydraulic conductivities. The lower conductivity region
423 around the coordinate $x = -50$ was reflected by verticalization of the DWL line. Maximum
424 and minimum calculated bulk resistivities (**Table 5**) correspond to, respectively, the clean
425 sandstone (facies 1 in **Table 3**) in the freshwater domain, and the clay facies in the saltwater
426 region.

427 In model #3, the computed width and penetration of the mixing zone were the lowest of
428 all the simulated models. The maximum resistivity value was, as in scenario #2, for the clean
429 sandstone in the freshwater region. The minimum value was obtained for the clay rich
430 sandstone in the saltwater region, although with lower clay content than facies 4 in model #2,
431 which produced the lowest resistivity value.

Table 5. *Characteristic values of resistivities and saltwater mixing zone geometrical indicators (i.e. SWI descriptors) obtained from application of the petrophysical model to the groundwater forward simulation. For those models with variable resistivities along the reference contours, max, min and mean values are shown. For the dyke scenario only max and min are shown for the 0.5 TDS resistivity.*

Model	W_{MZ} *(m)*	P_{Toe} *(m)*	P'_{DWL} *(m)*	Res_{Max} *(Ω·m)*	Res_{Min} *(Ω·m)*	Res_{DWL} *(Ω·m)*	$Res_{0.5\ TDS}$ *(Ω·m)*
#0	32.6	180.9	35.9	70.2	1.8	40.9	3.5
#1	89.7	129.6	46	24766	1.8	40.9	Max. (dyke) = 2506 Min. (sandstone) = 3.5
#2	20.7	117.2	47.8	195.3	1.1	Max. = 68.5 Min. = 7.3 Avg. = 27	Max. = 3.9 Min. = 1.9 Avg. = 3.1
#3	17.9	110.2	23.9	195.3	1.5	Max. = 56.9 Min. = 17.5 Avg. = 29.5	Max. = 3.9 Min. = 2.8 Avg. = 3.4

4.2 Errors associated with the petrophysical estimation of salinity from resistivity models

To assess in detail the errors associated with the estimation of salinity from the resistivity models using the transfer function we directly applied the petrophysical relationships, Archie and Waxman and Smits (section 3.4.2), to the true bulk resistivities to compute recovered water salinities. For both models since the heterogeneity is not known a priori we assumed homogeneous distribution of petrophysical parameters, here the values assigned to the reference sandstone (**Table 1** and **Table 4**). Additionally, for Waxman and Smits, we used a clay fraction value of 0.04.

Fig. 5 presents the comparison of true vs. recovered salinities, that is, the original salinities obtained from the groundwater model (**Fig. 5a, d**) compared to the salinities recovered from the resistivity models assuming petrophysical homogeneity (**Fig. 5b**, **d**). Relative errors, computed as the ratio between recovered over true TDS, show the over or underestimation of calculated salinity (**Fig. 5c, f**). Additionally, a summary of results is presented in **Table 6**.

Table 6. *SWI descriptors obtained from applying a homogeneous petrophysical relationship to the true resistivity sections. Error columns are differences between recovered values and the true simulated values compiled in* ***Table 5****.*

Model	***Petrophysical relationship***	W_{MZ}		P_{Toe}		P'_{DWL}	
		Recov.	*Error*	*Recov.*	*Error*	*Recov.*	*Error*
#0	*Archie*	31	-1.6	207.6	26.7	80.3	44.4
	Waxman and Smits	32.6	0	180.9	0	35.9	0
#1	*Archie*	91.8	2.1	132.6	3	91.4	45.4
	Waxman and Smits	89.7	0	129.6	0	46	0
#2	*Archie*	9.7	-11	117.6	0.4	47.9	0.1
	Waxman and Smits	9.6	-11.1	117.1	-0.1	47.3	-0.5
#3	*Archie*	15.1	-2.8	112.7	2.5	39.4	15.5
	Waxman and Smits	15	-2.9	112.5	2.3	37.1	13.2

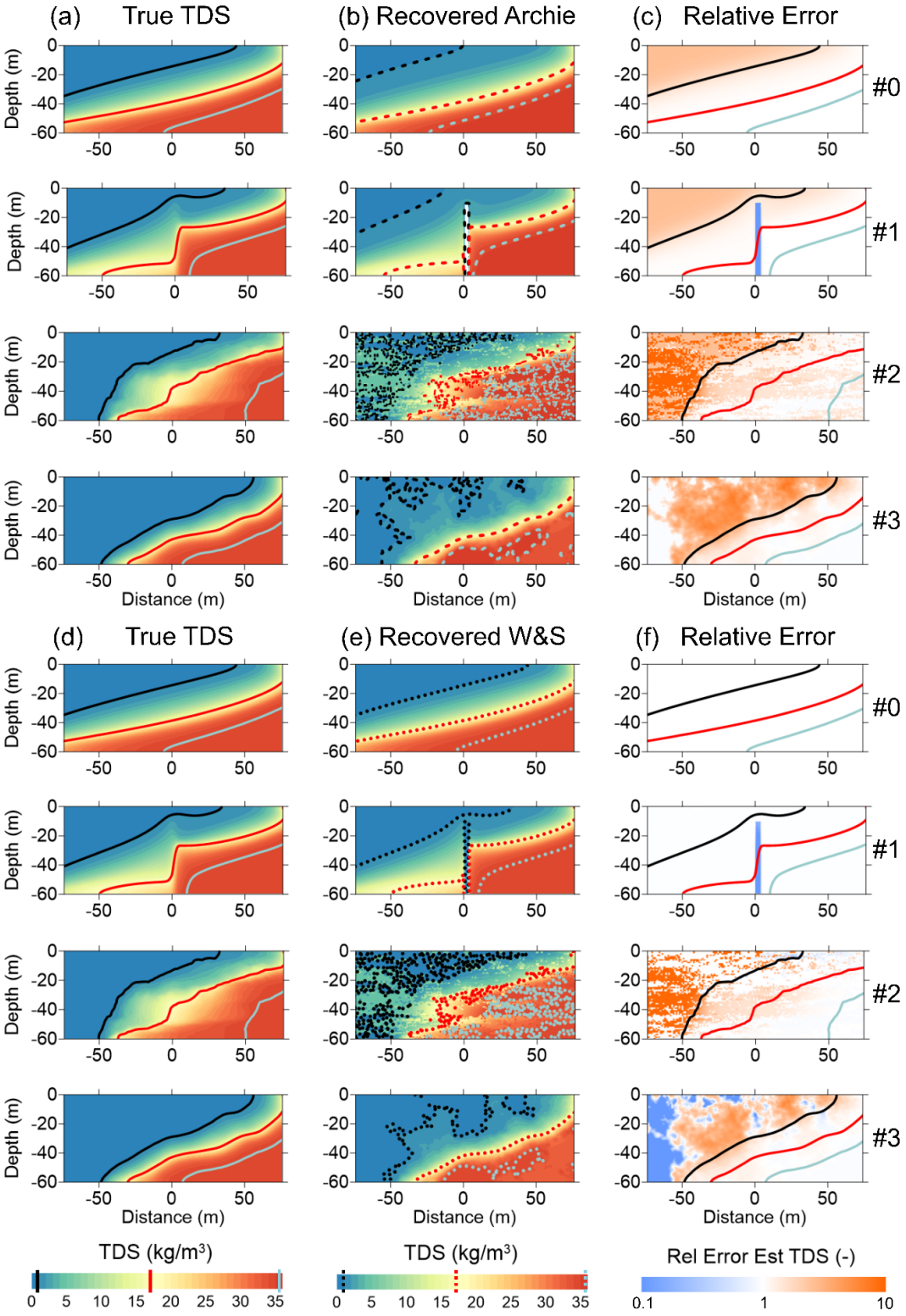

455

456 ***Fig. 5.*** *Results from application of homogeneous Archie* ***(b, c)*** *and Waxman and Smits (W&S)* ***(e, f)*** *to*
457 *the true bulk resistivities obtained in the forward models.* ***(a, d)*** *True (simulated) TDS.* ***(b, d)*** *Recovered*
458 *TDS.* ***(c, f)*** *Relative error, with values above 1 indicating higher recovered salinity than true value, and*

*values below indicating lower recovered value. Reference contours in all the sections are the same as in **Fig. 4** (dashed lines for Archie and dotted for Waxman and Smits).*

In the homogeneous model (#0), the use of Archie's model caused an overall overestimation of salinity content and encroachment reflected by higher penetration of the DWL line inland. The main discrepancies were observed in the freshwater region. No error were produced by application of Waxman and Smits, this because the model and parameters used to generate the true bulk resistivities were the same as in the forward model simulation.

Recovered salinity results from Archie for the dyke model #1 showed a similar trend as in scenario #0 for the low salinity domain. SWI descriptors (computed penetration and mixing zone width) exhibited higher values than the true model. The error was especially large for the DWL penetration, with an overestimation of 45.4 m. Waxman and Smits only produced errors in the dyke domain, but as described above for model scenario #0, not in the homogeneous sandstone.

The recovered TDS values for heterogeneous models (#2 and #3) illustrate the effect of the spatial variability. In model #2, the definition of facies led to a sharp transition of estimated TDS observed in **Fig. 5** with patchy contour delineation, both for Archie's and for Waxman and Smits petrophysical models. In the scenario model #3 the recovered salinity contours were smoother and more continuous than in model #2. However, a small low salinity isolated patch (with TDS<1) was observed near the surface towards the coast in both models. We considered this isolated patch as part of the freshwater region when computing the position of the DWL.

4.3 Errors associated with the inversion of resistivity measurements

The inverse resistivity models from true (but noised) ground measurements obtained for each forward model are compiled in **Table 7**. **Fig. 6** shows true (simulated in the forward

models) and recovered (inverted) resistivities for each studied scenario. Comparisons of fitting between true (simulated) and recovered (inverted) resistivities are also shown in **Fig. 8a**.

Table 7. *Summary statistics of the inverted models. λ denotes the regularization parameter for each model after using the L-curve criterion, RMS is the absolute root-mean square in Ω·m, RRMS is the relative RMS and Chi2 is the data misfit term (error-weighted sum of square errors) divided by the number of data. Error is the difference with the simulated true max and min resistivities as compiled in* ***Table 5****. Note that for model #1, because the dyke is not recovered, the difference in maximum resistivities is very large.*

Mesh		
	Nodes	***Cells***
Parameter Mesh	5809	11184
Secondary Mesh	22801	44736
Parameter Domain	4951	9393

Inversion Results								
Model	***λ***	***RMS (Ω·m)***	***RRMS (%)***	***Chi²***	***Res$_{Min}$ (Ω·m)***		***Res$_{Max}$ (Ω·m)***	
					Recovered	*Error*	*Recovered*	*Error*
#0	9.22	1.198	2.75	0.654	1.6	0.2	90.7	20.5
#1	11.53	1.17	3.461	0.879	2.4	0.6	82.8	-24683
#2	43.98	1.025	3.598	0.989	1.8	0.7	99.4	-95.9
#3	3.02	1.59	3.342	0.956	3	1.5	232.3	37

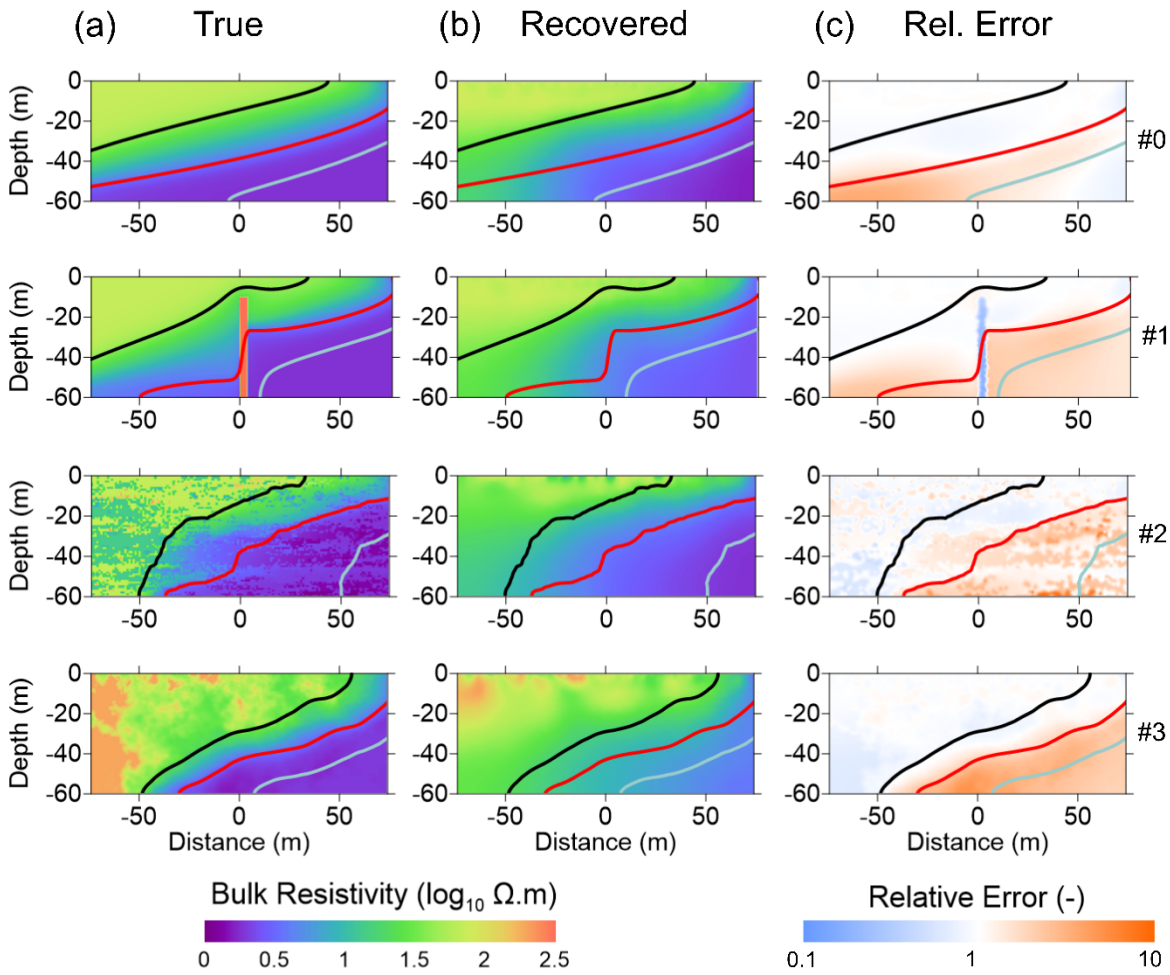

490

491 ***Fig. 6. (a)*** *True (simulated) bulk resistivity distributions.* ***(b)*** *Recovered inverted sections. Colormap is*
492 *the same for all resistivity models.* ***(c)*** *Relative error, computed as the ratio between recovered and true*
493 *resistivities, illustrate over and underestimation of recovered resistivities in the inversion. True TDS*
494 *contours are shown for reference.*

495 The general trend characterising all the recovered sections was a smoothening of
496 resistivity with increase in the saltwater domain (salinity values higher than 0.5, red contour
497 line in **Fig. 6**). Relative inversion errors were lower in freshwater regions, with a general
498 underestimation of resistivities (**Fig. 6c**). This was mainly due to the higher sensitivity and
499 resolution obtained near the surface, which is a known characteristic of electrical resistivity
500 imaging.

Inversion of model #0 overestimated maximum resistivities in the freshwater domain (higher recovered resistivity value of 90.7 Ω·m). In the region between the DWL and the central TDS contour (red line) the recovered values were very similar (although slightly lower) than the true resistivity distribution. In the saltwater domain however, the recovered resistivities were not as low as the true distribution. The absolute difference in this region was in the units of Ω·m, but, because of the low true values, the relative error was above 3. We identified the 0.5 salt mass fraction line as a central reference of dispersion of the inversion results, with a general underestimation of resistivities in the less saline (fresher) regions and overestimation of resistivities in the more saline regions (upper left and bottom right of **Fig. 6c** sections, respectively). This is, with some small-scale exceptions, a shared feature of all the models.

In the dyke example (#1) the inverted model failed to detect the dyke itself. Aside from that, the general patterns and trends of recovered resistivities were very similar to the inversion obtained for model #0. To the seaside of the dyke, relative errors higher than 1 did not extend above the 0.5 iso-contour, contrary to the inland side of the dyke (bottom left of sections in **Fig. 6c**).

Recovered sections from models #2 and #3 failed to reproduce the small-scale resistivity variations associated with the spatial distribution of the petrophysical properties. In model #2, the resolution decreases with depth where the inverted section was smoother, with poor recovery of resistivity variations. The true resistivity variability at small (metric) scale in the freshwater regions (left and upper left of the true section) was only recovered (yet with some dispersion) in the upper 10 m.

The general characteristics of model #3 are similar to the homogeneous model (**Fig. 6c**). We observed an overestimation of resistivities for higher salinities below the 0.5 line and slight underestimation towards the freshwater region. As for model #2, it was possible to delineate some of the general heterogeneities in the first 5-10 m, including a high resistivity, near surface

sandstone patch, although exhibiting a max resistivity value (232.3 Ω·m) higher than the true value.

4.4 Cumulative errors: salinity estimation from inverted ERI sections

In this section, we follow the same approach presented in section 4.2 to obtain a TDS distribution from the resistivity model but, instead of applying the petrophysical models over the true (simulated) bulk resistivities, we applied them to the recovered (inverted) resistivities and compare them to the true salinities obtained from the groundwater models. As in section 4.2 we assumed homogeneity in the petrophysical properties using parameters of the reference sandstone. The assumption of homogeneity is a common procedure applied in real-field situations where there is no direct information on the subsurface structure, and therefore the inverted resistivity sections are the only available information.

Fig. 7 shows a comparison of true (**Fig. 7a**, for Archie, and **Fig. 7d**, for Waxman and Smits) and recovered (**Fig. 7b**, **e**) salinity (TDS) sections for the four models. **Fig. 7c** and **Fig. 7f** show the relative errors calculated with estimated over true TDS distribution for Archie and Waxman and Smits respectively. We used the same SWI descriptors presented in section 4.1, including the error defined as the absolute difference between estimated and true values. Results are compiled in **Table 8**. For some models reference TDS iso-contours were not recovered. In these models (marked with an asterisk in **Table 8**) W_{MZ} is computed as the distance at the bottom of the aquifer between the 0.25 iso-concentration and the maximum x-coordinate of the recovered section ($x = 76$ m). In model #3 the 0.5 salinity contour was not recovered so results for P_{Toe} are not included.

Table 8. *SWI descriptors obtained from salinity sections derived from the inverted resistivity section using a homogeneous petrophysical relationship. Error columns indicate the differences between recovered values and the true simulated values compiled in* ***Table 5****. Positive errors in* P_{Toe} *and* P'_{DWL} *mean overestimation of SWI penetration (towards inland) while negative values underestimation (contours towards the sea).*

Model	***Petrophysical relationship***	W_{MZ}		P_{Toe}		P'_{DWL}	
		Recov.	*Error*	*Recov.*	*Error*	*Recov.*	*Error*
#0	*Archie*	44.6	12	90.9	-90	67.2	31.3
	Waxman and Smits	44.7	12.1	89.2	-91.7	33.2	-2.7
#1	*Archie*	79.2	-10.5	68	-61.6	79.9	33.9
	Waxman and Smits	87.1*	-2.5	66	-63.6	43.1	-2.9
#2	*Archie*	57.3	36.6	84.3	-32.9	64.5	16.7
	Waxman and Smits	57.2	36.5	82.8	-34.4	45.2	-2.6
#3	*Archie*	63*	45.1	-	-	43.6	19.7
	Waxman and Smits	53.6*	35.7	-	-	36.4	12.5

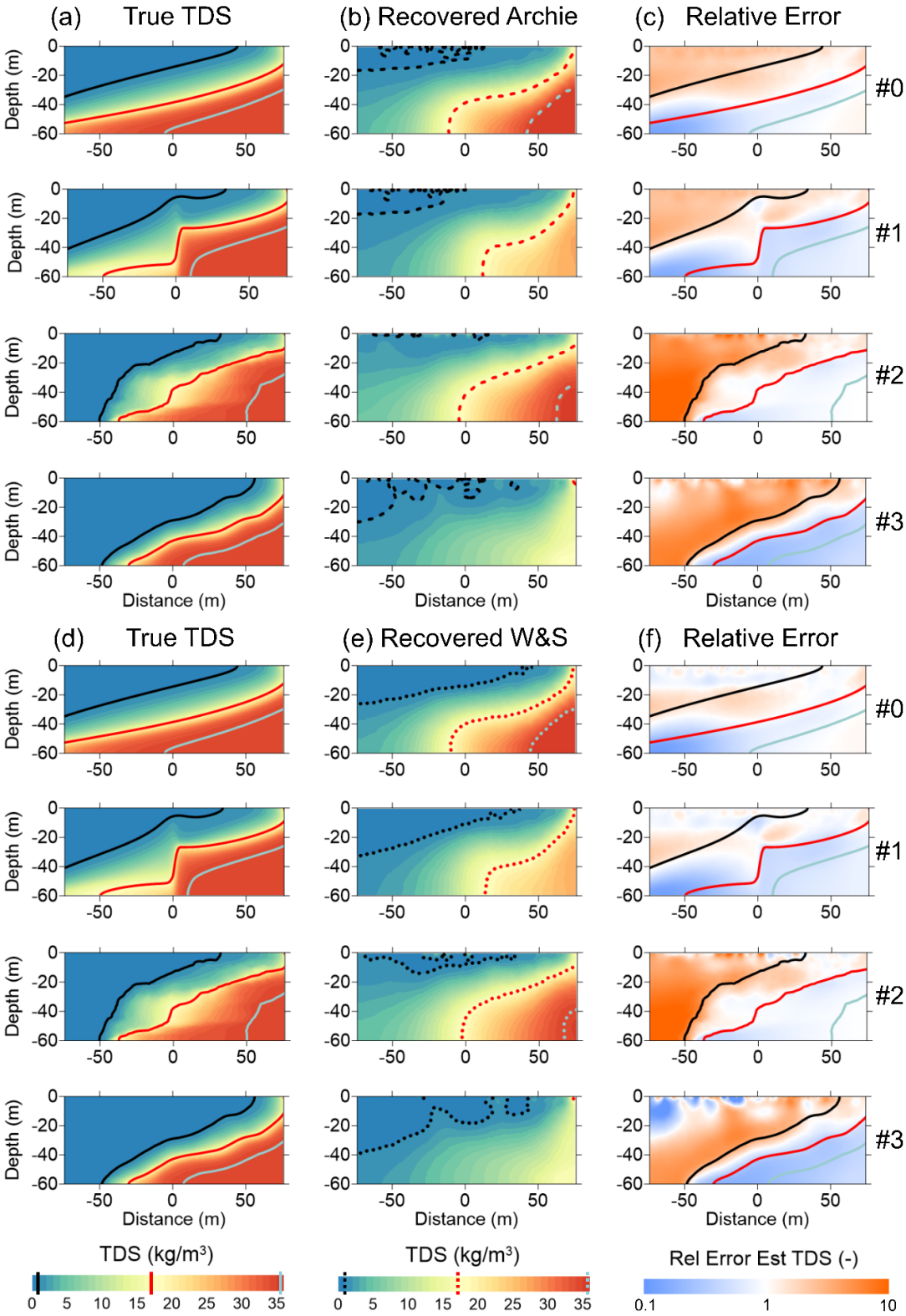

553

554 ***Fig. 7.*** *Comparison between* ***(a, d)*** *true (simulated) TDS and* ***(b, e)*** *TDS recovered from inversion using*
555 *homogeneous Archie* ***(b)*** *and Waxman and Smits (W&S)* ***(e)****, and associated relative errors* ***(c, f)****.*

In the homogeneous scenario, model #0, the recovered salinities from the inverted resistivity models show smoother and more diffuse patterns than the true TDS distributions obtained from the groundwater simulation. Both Archie and Waxman and Smits resulted in similar values of computed mixing zone width and toe penetration. Application of Waxman and Smits resulted in much lower cumulative errors in the definition of the tip of the mixing zone.

In the dyke model (#1), the mixing zone width, for estimation using either Archie or Waxman and Smits models, was lower than the true simulation reference values. This might have been caused by the overestimation of resistivity values in the inversion in the inland side of the dyke, which after applying the petrophysical models led to an apparent reduction of mixing zone thickness.

In the heterogeneous scenarios (#2 and 3) we obtained similar results regarding the general characteristics because of the cumulated effect of the inversion and petrophysical relationship. As in the homogeneous model, we observed a widening of the mixing zone and an underestimation of toe penetration. It should be noted that the definition of P'_{DWL} was complex as the results were observed as unconnected bubbly iso-contours. For the scenario #3, the toe penetration and the width of the mixing zone descriptor were not fully obtained as the 0.5 and 0.75 salinity concentrations were not recovered. In this model both petrophysical models overestimated the position of the DWL.

The dispersion effect for salinity estimation, caused mainly by the smooth inversion, was found to be more important in the lower TDS domain, while the selection of the petrophysical model influenced the accurate delineation and location of the P'_{DWL}. **Fig. 8** shows scatter plots of recovered values from inversion and cumulated (inversion and petrophysical) versus true simulated values in resistivity and TDS. The coverage shows the sensitivity of the recovered value in the resistivity inversion. Generally, lower coverage values were obtained in the deeper

581 domains of the model and reflect less constrained model cells, especially in the saltwater
582 domain. This was clearly observed in the homogeneous model #0. In model #1 the dyke was
583 not recovered at all, however, this did not translate into the TDS estimation as the real salinity
584 distribution was smoother. A general result was that Waxman and Smits homogenous
585 estimations, in general, produced better fits to true data, although this was expected because
586 this model was the one used to simulate the forward responses. However, in the heterogeneous
587 models #2 and #3, Waxman and Smits led to underestimation of TDS in the lowest salinity
588 regions.

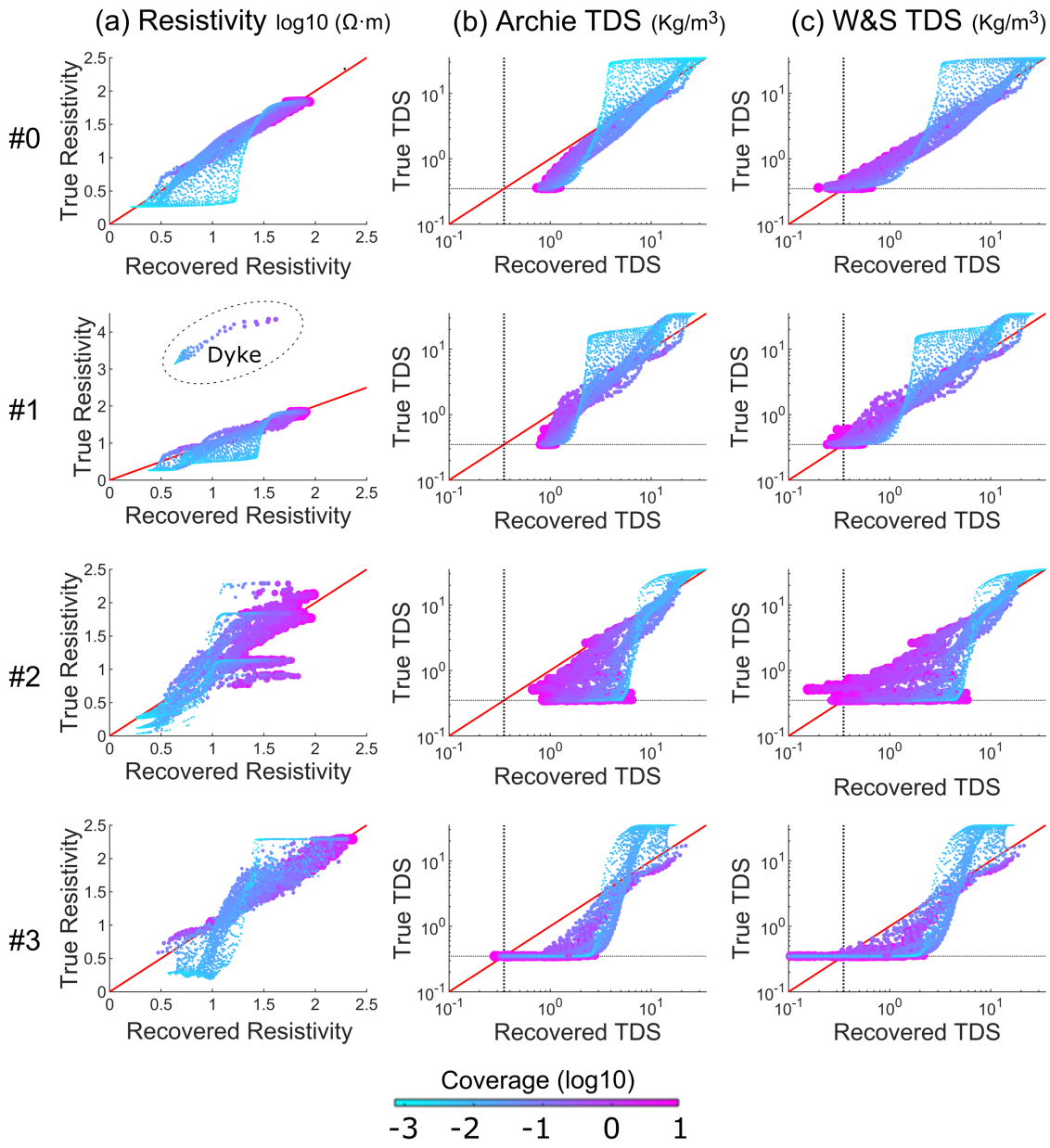

589

590 ***Fig. 8.*** *Adjustment between true and recovered resistivities* ***(a)*** *and true and recovered TDS using*
591 *homogeneous Archie* ***(b)*** *and Waxman and Smits* ***(c)*** *petrophysical relationships. The horizontal and*
592 *vertical dotted black lines indicate the lowest limit of true salt mass fraction (TDS=0.35 kg* m^{-3}*, see*
593 *section 3.2). Red line is 1:1. Higher sensitivity (coverage) cells in the inverted resistivity models are*
594 *represented with larger markers and purple colors.*

5 Discussion

5.1 Impact of petrophysical model selection in the delineation of SWI

The use of an appropriate petrophysical transfer function is crucial in hydrogeophysics. In the examples shown in this work, a clearly observed effect is that the reference freshwater limit (DWL) was systematically located further inland as compared to its true position. **Fig. 9** shows the estimated position of reference contours obtained from the conversion into salinities of the recovered electrical inverted sections. Additionally, the error associated with the petrophysical conversion was for all the models amplified by the smoothness associated to the inversion itself. Recent works (Revil et al., 2017) pointed out that, although the use of existing alternative and more accurate relationships is increasing in field-based hydrogeophysical studies, there is still a significant number of reports in which Archie's has been improperly applied leading to incorrect interpretation.

In this work we used the Waxman and Smits model because, conceptually, it can be easily compared with the extensively used Archie's model to evaluate the importance of accounting for clay content. Alternative models, more theoretically grounded and versatile (e.g. Bussian, 1983; Revil et al., 1998, 2018) are available and should be also evaluated. Nevertheless, in a real-case field situation where there is no direct information on the presence and amount of clay, and, therefore, no argument supporting the selection of the appropriate petrophysical relationship, we suggest that the choice depends on the practical aim of the study. More specifically, we have observed that Waxman and Smits may tend to provide some underestimation of real TDS (see for example points above the 1:1 line in **Fig. 8**) while Archie tends to significantly overestimate TDS with larger errors. This implies that in a real-world scenario, the use of Waxman and Smits would be on the risk side of the spectrum, that is, leading to underestimating the risk and imminence of saltwater intrusion. In such case, if the

study aims at safe freshwater abstraction and protection against saltwater intrusion it would be preferable to use Archie's equation, because it exaggerates the proximity of saltwater and therefore provides a security margin with respect to the risk of salinization. However, when the study aims at accurately delineating saltwater intrusion or optimizing freshwater use, particularly in relatively brackish environments (e.g. arid and/or tropical regions, small islands), and/or at better understanding the dynamic processes associated with the transition zone itself or the saline parts of the aquifer, a petrophysical relationship accounting for clay content (Waxman and Smits or others) would provide quantitatively more accurate and reliable results. When applying one of these models, the estimation of TDS in the low salinity (high resistivity) region is highly sensitive to clay content: the higher the clay fraction in the transfer function, the deeper the estimated DWL and the further towards the coast. Practically, in a scenario with lower clay or clay-free content, the petrophysical assumption of higher clay fraction would lead to incorrect, and detrimental, estimation of the DWL located further towards the sea.

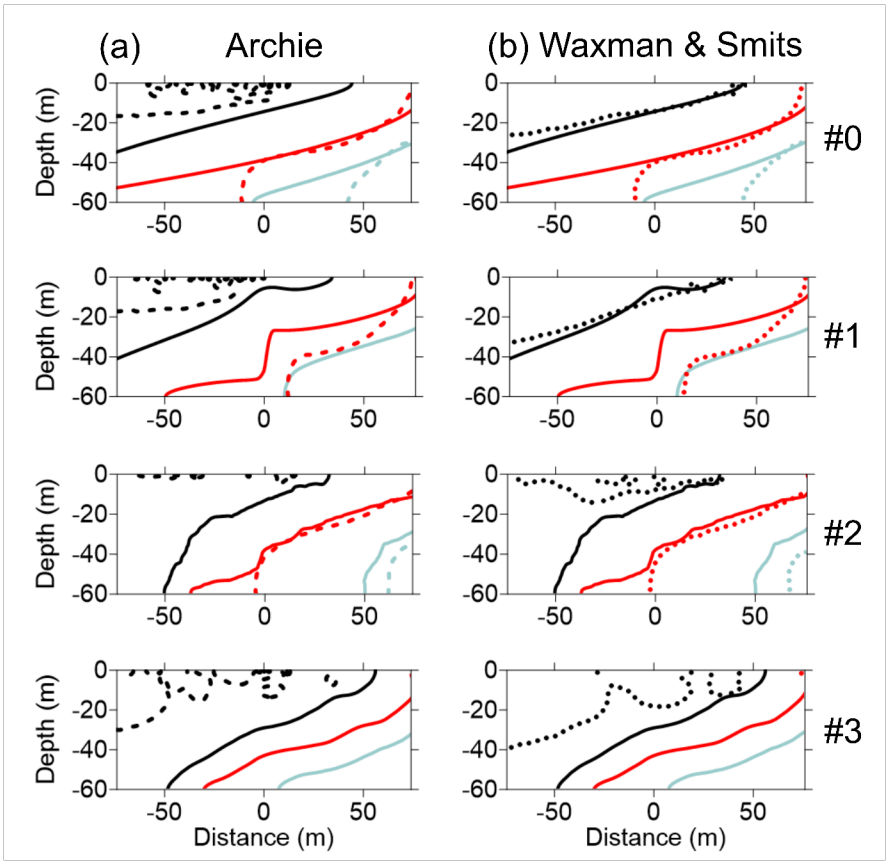

633

634 ***Fig. 9.*** *Comparison of estimation of TDS reference iso-contours after applying Archie (a; dashed lines)*
635 *and Waxman and Smits (b; dotted lines) petrophysical relationships to the inverted resistivity sections.*
636 *Reference true contours are indicated as plain lines.*

637 ## 5.2 Inconsistencies of surface ERI with borehole data

638 Discrepancies (usually underestimation) between salinity estimated from surface ERI
639 and salinities (or electrical resistivities/conductivities) measured in boreholes, as well as
640 between surface and borehole resistivity data, have been observed in some real-world
641 experiences (e.g. Goebel et al., 2017, Palacios et al., 2020). This is because the depth-resolution
642 limitation of surface ERI overrides and smooths small-scale geological variations.

643 In **Fig. 10** we illustrate and compare the results assuming the availability of borehole
644 data extracted in vertical profiles of true (modelled) reference resistivity and salinity (TDS) at
645 coordinate $x = 0$ for each model (virtual borehole in **Fig. 2**). This information was plotted
646 along with recovered logs obtained from the inverted section and application of the

647 petrophysical relationships to the inverted resistivities. The comparisons illustrate more
648 specifically the impact of the cumulated errors on final estimation when typically reconciling
649 geophysical results to borehole logs.

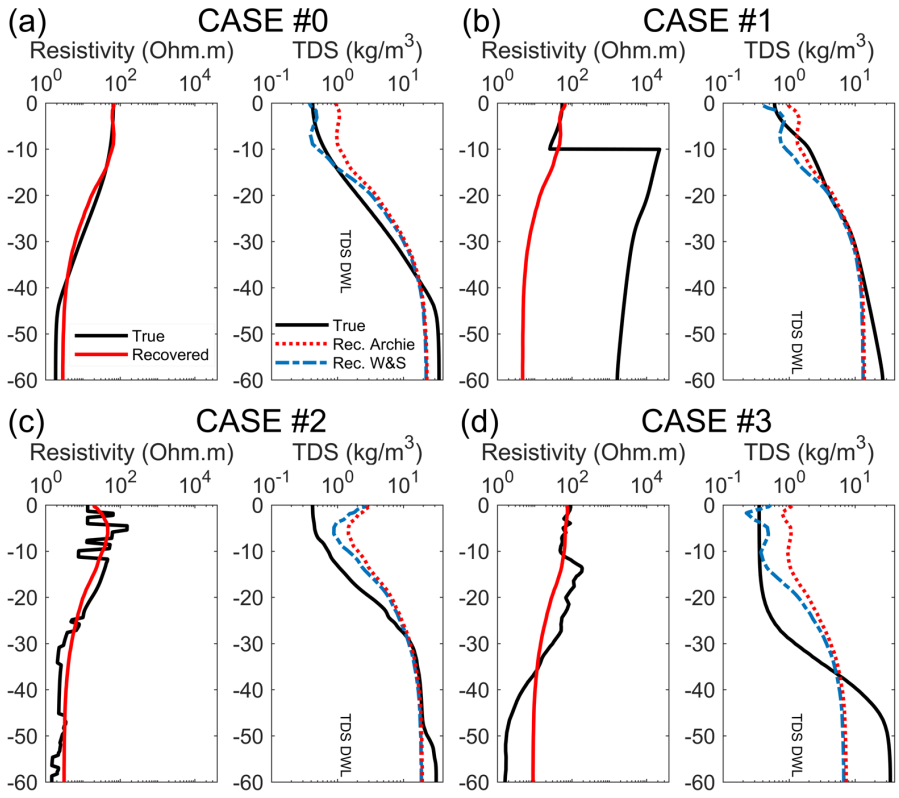

650

651 ***Fig. 10.*** *Vertical profiles at coordinate x=0 of true vs. inverted resistivities (left) and true vs. recovered*
652 *(using Archie and Waxman and Smits) salinity concentration in TDS (right) for each scenario. The*
653 *vertical dotted line denotes the DWL (TDS=1 kg m^{-3}).*

654 Waxman and Smits, and more so Archie, tended to overestimate the salinity content in
655 near-surface low salinity regions for all models with the exception of model #1 for Waxman
656 and Smits. At the opposite, they both tended to underestimate TDS in deeper high salinity
657 regions. These result from the smoothing effect of the inversion itself (and its inability to
658 recover some deep extreme values) and the petrophysical homogeneity assumption when
659 converting inverted resistivity to TDS (which adds to the inversion errors as shown when
660 comparing true vs recovered TDS).

To address the inversion smoothing effect with depth near boreholes, previous authors (e.g. Palacios et al., 2020) suggested, when available, to jointly invert surface and cross-hole electrical resistivity tomography, which increases depth resolution and provides better imaging of saltwater intrusion. Alternatively, incorporating salinity and geophysical data within a coupled hydrogeophysical inversion framework (e.g. Kang et al., 2019) can also address the overdispersion as the groundwater model acts as physically-based regularization (e.g. Camporese et al., 2015). In any case, the use of borehole salinity (or electrical conductivity) measured in boreholes (especially fully screened wells) is also subject to errors (e.g. Shalev et al., 2009; Carrera et al., 2010) that should be appropriately assessed.

5.3 Effect of heterogeneity in the petrophysical estimation

In real world practical hydrogeological applications, heterogeneity is a widespread natural characteristic of aquifers which exerts a strong influence on groundwater flow and solute transport, including saltwater intrusion. When using geophysical methods for delineating seawater intrusion in heterogeneous coastal aquifers, their interpretation should not only focus on fluid salinity, but should also consider the aquifer's petrophysical properties, in order to avoid incorrect interpretations of salt distribution particularly in the lowest salinity regions. The results presented in this work suggest that significant errors can be made by relating an iso-resistivity value directly to a fluid salinity contour in naturally heterogeneous and/or clayed environments, with errors increasing with the degree of heterogeneity and amount of clay (**Fig. 8**).

Additional errors add up when electrical properties obtained after inversion are transformed into hydrogeological variables if geological variability is not properly recovered or accounted for in the petrophysical model. The resolution limitations and scale effects in petrophysical estimation from geophysical tomograms has been highlighted by previous

685 authors (e.g. Day-Lewis et al., 2005; Singha and Moysey, 2006). Further research is necessary
686 to evaluate in more detail the effect of the different types of heterogeneities and the relation
687 between property variation scales and resolution of the geophysical method and provide
688 alternative methodologies to improve the estimation of properties from electrical tomograms
689 (e.g. Nussbaumer et al., 2019). In the context of SWI, this effect is of great importance as it has
690 been observed that small scale heterogeneities may exert an important control in the spreading
691 and characteristics of the mixing zone (Kerrou and Renard, 2010; Yu and Michael, 2019).

692 To increase resolution of small-scale heterogeneity by resistivity imaging, an alternative
693 would be to reduce electrode spacing, but this in practice would result in a lower depth of
694 investigation because most resistivity arrays have a limited number of electrode takeouts,
695 which in turn would increase the uncertainty in identifying the delineation of the seawater
696 intrusion at depth. In this work, we performed the analysis using a Wenner-alpha electrode
697 array –chosen for having a high signal-to-noise-ratio in real world settings— with a pre-defined
698 electrode spacing of 2 m. The use of alternative and/or combined electrode arrays and spacing
699 can improve recovered images and reduce the final cumulated error (Comte, 2009). Forward
700 coupled models are able to provide support for pre-survey evaluation of the most optimal
701 array(s) (Wilkinson et al., 2006) using a conceptualization of the heterogeneous scenario and
702 expected hydrogeological settings. Multi-scale surveys (combining different small and large
703 electrode spacing) and combination with cross-hole electrical resistivity tomography (Palacios
704 et al., 2020) would be beneficial in enhancing depth resolution.

705 After data collection, the analysis of resistivity data may also benefit from the use of
706 appropriate appraisal tools (Oldenburg and Li, 1999; Caterina et al., 2013). Additionally,
707 hydrogeophysical SWI studies would be improved by performing uncertainty analysis (Linde
708 et al., 2017), including the evaluation of uncertainty associated to the petrophysical model in
709 the transfer of information between the hydrogeological and geophysical models (Brunetti and

710 Linde, 2018). The results presented in this work suggest that, even for acceptable values of
711 sensitivity, hydrogeological information derived from geophysics must be used with caution in
712 the calibration of groundwater models, especially in heterogeneous aquifers. Although there is
713 a relationship between geological properties and salinity distribution, and the electrical signal
714 collected by electrical resistivity devices, the transfer of information requires a series of steps
715 in which errors might cumulate and lead to interpretation biases. Erroneous (or oversimplified)
716 conceptualization of the hydrogeological model, use of an incorrect petrophysical relationship
717 or the limitations in the geophysical inversion may introduce important errors, especially for
718 the calibration of groundwater models with geophysically-derived salinity. The use of fully-
719 coupled hydrogeophysical inversion is a way forward to overcome these limitations (Comte
720 and Banton, 2007; Hinnell et al., 2010; Linde and Doestch, 2016). Coupled models guarantee
721 that the geophysical response respects the hydrogeological processes (including unconfined
722 conditions and variable saturation), honours a better correspondence between the distribution
723 of geological properties and the application of petrophysical models, allowing for the
724 introduction of geological realistic models in the whole procedure (Linde et al., 2015) and have
725 the potential to incorporate additional geophysical techniques such as gravimetry (González-
726 Quirós and Fernández-Álvarez, 2017), electromagnetics (Qi et al., 2019) or self-potential
727 (Graham et al., 2018). On the other hand, coupled models generally have a higher
728 computational cost that can be an important limiting factor in some applications. Finally, and
729 perhaps most importantly, any numerical model and inversion procedure, either coupled or not,
730 cannot overcome a wrong system conceptualization (Carrera et al., 2010). Its definition and
731 selection should be integrated in the modelling and inversion workflow (Linde, 2014; Brunetti
732 et al., 2019).

6 Conclusions

The use of electrical and electromagnetic methods, which both provide information on subsurface resistivity, has proven effective for the qualitative delineation and mapping of saltwater distribution in coastal aquifers. The quantitative use of resistivity data in heterogeneous aquifer systems, where resistivity variations are both controlled by salinity and lithology variations, requires a good understanding of both geophysical inversion and petrophysical model capabilities and limitations. In this paper we have shown some of the limitations and complexities in the geoelectrical data interpretation in heterogeneous coastal aquifers using the capabilities of a fully-coupled finite element hydrogeophysical model.

Through considering a range of plausible hydrogeological models with various degree of heterogeneity, we have illustrated some of the resolution problems that can be encountered in real-world coastal aquifer applications when interpreting inverted geophysical data in terms of pore water salinity distribution. For a constant fluid conductivity, variations of resistivity of more than one order of magnitude associated to variations of petrophysical parameters (porosity, clay content, cementation factor) are possible, particularly in low salinity regions. This may introduce significant errors when using resistivity models to map drinking water salinity thresholds. As a result, direct use of a constant resistivity threshold to delineate seawater intrusion positions should be avoided without additional information about the geological heterogeneity of the aquifer. Geological property variability influences the geoelectrical signal and might lead to erroneous interpretations of resistivity variations as overly complex seawater intrusion patterns instead of a combination of geological and salinity variability. This might lead to important errors that can be introduced when electrical resistivity data is used at any stage of the hydrogeological study, from the qualitative interpretation of electrical images for site conceptualization to the quantitative use of resistivity-derived salinity data for groundwater model calibration.

From a methodological point of view, the presented coupled multiphysics modelling approach can be further used to assess the sensitivity of, and optimise, various geoelectrical electrode arrays and time-lapse acquisition procedure most suited to specific types of geological heterogeneity and hydrogeological scenarios, including for example, topographic effects, pumping and other transient boundary conditions. The methodology can be expanded to incorporate variable saturation in the groundwater model as well as other geophysical methods, such as electromagnetics (e.g. FEM, TEM). Of particular interest is the analysis of three-dimensional effects (boundary conditions, heterogeneities) which add technical challenges in the geophysical imaging capabilities and interpretation. The approach can be highly beneficial prior to a field survey, through assisting the design of optimal, cost-effective field campaigns as well as preventing excessive expectations (from both the geophysicist and the client) about the capabilities of geophysics to identify subsurface features. It also allows for including specific threshold salinity values as defined by water managers depending on their needs. This provides an additional methodology for integration of DC resistivity data into early warning systems for SWI identification and in groundwater models used for decision-making in the management of freshwater resources of coastal aquifers.

7 Acknowledgments

Andrés González Quirós is the recipient of a Royal Society – Newton International Fellowship (NIF\R1\182210), hosted at the University of Aberdeen. We thank two anonymous reviewers for their constructive comments, which contributed to improve the manuscript.

8 References

Archie, G. E. (1942). The electrical resistivity log as an aid in determining some reservoir characteristics. Transactions of the AIME, **146**(01), 54-62.

781 Bear, J., & Cheng, A. H. D. (2010). Modeling groundwater flow and contaminant transport.
782 Springer.

783 Beaujean, J., F. Nguyen, A. Kemna, A. Antonsson, and P. Engesgaard (2014). Calibration of
784 seawater intrusion models: Inverse parameter estimation using surface electrical
785 resistivity tomography and borehole data. *Water Resources Research*, **50**, 6828–6849.
786 https://doi.org/10.1002/2013WR014020

787 Berg, C. R., (1995). A simple effective-medium model for water saturation in porous rocks:
788 *Geophysics*, **60**, 1070–1080, https://doi.org/10.1190/1.1443835

789 Binley, A., Cassiani, G., & Deiana, R. (2010). Hydrogeophysics: opportunities and challenges.
790 *Bollettino di Geofisica Teorica ed Applicata*, **51**(4).

791 Binley, A., Hubbard, S. S., Huisman, J. A., Revil, A., Robinson, D. A., Singha, K., & Slater,
792 L. D. (2015). The emergence of hydrogeophysics for improved understanding of
793 subsurface processes over multiple scales. *Water Resources Research*, **51**(6), 3837-3866.
794 https://doi.org/10.1002/2015WR017016

795 Blome, M., Maurer, H. R. & Schmidt, K. (2009). Advances in three-dimensional geoelectric
796 forward solver techniques. *Geophysical Journal International*, **176(**3), 740-752.
797 https://doi.org/10.1111/j.1365-246X.2008.04006.x

798 Brunetti, C., Linde, N., & Vrugt, J. A. (2017). Bayesian model selection in hydrogeophysics:
799 Application to conceptual subsurface models of the South Oyster Bacterial Transport
800 Site, Virginia, USA. *Advances in Water Resources*, **102**, 127-141.
801 https://doi.org/10.1016/j.advwatres.2017.02.006

802 Brunetti, C., & Linde, N. (2018). Impact of petrophysical uncertainty on Bayesian
803 hydrogeophysical inversion and model selection. *Advances in Water Resources*, **111**,
804 346-359. https://doi.org/10.1016/j.advwatres.2017.11.028

805 Brunetti, C., Bianchi, M., Pirot, G., & Linde, N. (2019). Hydrogeological model selection
806 among complex spatial priors. *Water Resources Research*, **55**(8), 6729-6753.
807 https://doi.org/10.1029/2019WR024840

808 Bussian, A. E. (1983). Electrical conductance in a porous medium. Geophysics, **48**(9), 1258-
809 1268. https://doi.org/10.1190/1.1441549

810 Butler, S. L., & Sinha, G. (2012). Forward modeling of applied geophysics methods using
811 Comsol and comparison with analytical and laboratory analog models. *Computers &*
812 *Geosciences*, **42**, 168-176. https://doi.org/10.1016/j.cageo.2011.08.022

813 Cai, J., Wei, W., Hu, X., & Wood, D. A. (2017). Electrical conductivity models in saturated
814 porous media: A review. *Earth-Science Reviews*, **171**, 419-433.
815 https://doi.org/10.1016/j.earscirev.2017.06.013

816 Camporese, M., Cassiani, G., Deiana, R., Salandin, P., & Binley, A. (2015). Coupled and
817 uncoupled hydrogeophysical inversions using ensemble K alman filter assimilation of
818 ERT-monitored tracer test data. *Water Resources Research*, **51**(5), 3277-3291.
819 https://doi.org/10.1002/2014WR016017

820 Carrera, J., Hidalgo, J. J., Slooten, L. J., & Vázquez-Suñé, E. (2010). Computational and
821 conceptual issues in the calibration of seawater intrusion models. *Hydrogeology Journal*,
822 **18**(1), 131-145. https://doi.org/10.1007/s10040-009-0524-1

823 Caterina, D., Beaujean, J., Robert, T., & Nguyen, F. (2013). A comparison study of different
824 image appraisal tools for electrical resistivity tomography. *Near Surface Geophysics*,
825 **11**(6), 639-657. https://doi.org/10.3997/1873-0604.2013022

826 Comte, J. C., & Banton, O. (2007). Cross-validation of geo-electrical and hydrogeological
827 models to evaluate seawater intrusion in coastal aquifers. *Geophysical Research Letters*,
828 **34**(10). https://doi.org/10.1029/2007GL029981

829 Comte J. C. (2009) Contribution of electrical resistivity tomography to variable-density
830 groundwater flow modelling in coastal aquifers – Application to three contrasted climate
831 settings (Canada, New Caledonia, Senegal), PhD thesis, University of Avignon.

832 Comte, J. C., Wilson, C., Ofterdinger, U. and González-Quirós, A. (2017). Effect of volcanic
833 dykes on coastal groundwater flow and saltwater intrusion: A field-scale multiphysics
834 approach and parameter evaluation. *Water Resources Research*, **53**(3), 2171-2198.
835 https://doi.org/10.1002/2016WR019480

836 Constable, S. C., Parker, R. L., & Constable, C. G. (1987). Occam's inversion: A practical
837 algorithm for generating smooth models from electromagnetic sounding data.
838 Geophysics, 52(3), 289-300. https://doi.org/10.1190/1.1442303

839 Day-Lewis, F. D., Singha, K., & Binley, A. M. (2005). Applying petrophysical models to radar
840 travel time and electrical resistivity tomograms: Resolution-dependent limitations.
841 Journal of Geophysical Research: Solid Earth, 110(B8).
842 https://doi.org/10.1029/2004JB003569

843 De Franco, R., Biella, G., Tosi, L., Teatini, P., Lozej, A., Chiozzotto, B., Giada, M., Rizzeto,
844 F., Claude, C., Mayer, A., Bassan, V. & Gasparetto-Stori, G. (2009) Monitoring the
845 saltwater intrusion by time lapse electrical resistivity tomography: the Chioggia test site
846 (Venice Lagoon, Italy). *Journal of Applied Geophysics*, **69**(3-4), 117–30.
847 https://doi.org/10.1016/j.jappgeo.2009.08.004

848 Dey, A., and Morrison, H. F. (1979). Resistivity modelling for arbitrarily shaped two-
849 dimensional structures. *Geophysical Prospecting*, **27**(1), 106-136.
850 https://doi.org/10.1111/j.1365-2478.1979.tb00961.x

851 Ferre, T., Bentley, L., Binley, A., Linde, N., Kemna, A., Singha, K., Holliger, K., Huisman, J.
852 A., & Minsley, B. (2009). Critical steps for the continuing advancement of

hydrogeophysics, *EOS Trans*actions American Geophysical Union, **90**(23), 200. https://doi.org/10.1029/2009EO230004

Glover, P. (2009). What is the cementation exponent? A new interpretation. *The Leading Edge*, **28**(1), 82-85. https://doi.org/10.1190/1.3064150

Goebel, M., Pidlisecky, A., & Knight, R. (2017). Resistivity imaging reveals complex pattern of saltwater intrusion along Monterey coast. Journal of Hydrology, 551, 746-755. https://doi.org/10.1016/j.jhydrol.2017.02.037

Gómez-Hernández, J. J., & Srivastava, R. M. (1990). ISIM3D: An ANSI-C three-dimensional multiple indicator conditional simulation program. *Computers & Geosciences*, **16**(4), 395-440. https://doi.org/10.1016/0098-3004(90)90010-Q

Gómez-Hernández, J. J., & Journel, A. G. (1993). Joint Sequential Simulation of MultiGaussian Fields. In: Soares A. (eds) *Geostatistics Tróia '92. Quantitative Geology and Geostatistics*, **5**. Springer, Dordrecht. https://doi.org/10.1007/978-94-011-1739-5_8

González-Quirós, A., & Fernández-Álvarez, J. P. (2017). Forward Coupled Modeling and Assessment of Gravity Anomalies Caused by Pumping Tests in Unconfined Aquifers Under Unsteady-State Conditions. *Mathematical Geosciences*, **49**(5), 603-617. https://doi.org/10.1007/s11004-016-9634-1

González-Quirós, A., Comte, J., Rubio-Melendi, D., & Fernández-Álvarez, J. (2019). Towards fully coupled finite element modelling of DC resistivity in complex seawater intrusion scenarios. 81st EAGE Conference and Exhibition 2019, London. https://doi.org/10.3997/2214-4609.201900972

Graham, M. T., MacAllister, D. J., Vinogradov, J., Jackson, M. D., & Butler, A. P. (2018). Self-potential as a predictor of seawater intrusion in coastal groundwater boreholes. Water Resources Research, 54(9), 6055-6071. https://doi.org/10.1029/2018WR022972

Günther, T., Rücker, C., & Spitzer, K. (2006). Three-dimensional modelling and inversion of DC resistivity data incorporating topography—II. Inversion. *Geophysical Journal International*, **166**(2), 506-517. https://doi.org/10.1111/j.1365-246X.2006.03011.x

Günther, T. & Rücker, C (2019). Boundless Electrical Resistivity Tomography BERT v2.2 – the user tutorial, LIAG Hannover, TU Berlin. Available at: http://www.resistivity.net/download/bert-tutorial.pdf (last access: 7 January 2020).

Hem, J. D. (1985). Study and interpretation of the chemical characteristics of natural water (Vol. 2254). Department of the Interior, US Geological Survey.

Henry, H. R. (1964). Effects of dispersion on salt encroachment in coastal aquifers, in" Seawater in Coastal Aquifers. US Geological Survey, *Water Supply Paper*, **1613**, C70-C80.

Hinnell, A. C., Ferré, T. P. A., Vrugt, J. A., Huisman, J. A., Moysey, S., Rings, J. & Kowalsky, M. B. (2010). Improved extraction of hydrologic information from geophysical data through coupled hydrogeophysical inversion. *Water Resources Research*, **46**(4). https://doi.org/10.1029/2008WR007060

Houben, G. J., Stoeckl, L., Mariner, K. E., & Choudhury, A. S. (2018). The influence of heterogeneity on coastal groundwater flow-physical and numerical modeling of fringing reefs, dykes and structured conductivity fields. *Advances in Water Resources*, **113**, 155-166. https://doi.org/10.1016/j.advwatres.2017.11.024

Jiao, J., & Post, V. (2019). Coastal Hydrogeology. Cambridge University Press. https://doi.org/10.1017/9781139344142

Journel, A.G. (1989). Fundamentals of Geostatistics in Five Lessons. Volume 8 of Short Courses in Geology. AGU, Washington D.C.

Kang, X., Shi, X., Revil, A., Cao, Z., Li, L., Lan, T., & Wu, J. (2019). Coupled hydrogeophysical inversion to identify non-Gaussian hydraulic conductivity field by jointly assimilating geochemical and time-lapse geophysical data. *Journal of Hydrology*, **578**, 124092. https://doi.org/10.1016/j.jhydrol.2019.124092

Kerrou, J., & Renard, P. (2010). A numerical analysis of dimensionality and heterogeneity effects on advective dispersive seawater intrusion processes. *Hydrogeology Journal*, 18(1), 55-72. https://doi.org/10.1007/s10040-009-0533-0

Kerrou, J., Renard, P., Cornaton, F., & Perrochet, P. (2013). Stochastic forecasts of seawater intrusion towards sustainable groundwater management: application to the Korba aquifer (Tunisia). *Hydrogeology Journal*, 21(2), 425-440. https://doi.org/10.1007/s10040-012-0911-x

Kirkegaard, C., Sonnenborg, T. O., Auken, E., & Jørgensen, F. (2011). Salinity distribution in heterogeneous coastal aquifers mapped by airborne electromagnetics. *Vadose Zone Journal*, **10**(1), 125-135. https://doi.org/10.2136/vzj2010.0038

Koltermann, C. E., & Gorelick, S. M. (1996). Heterogeneity in sedimentary deposits: A review of structure-imitating, process-imitating, and descriptive approaches. *Water Resources Research*, **32**(9), 2617-2658. https://doi.org/10.1029/96WR00025

Lesmes, D. P., & Friedman, S. P. (2005). Relationships between the electrical and hydrogeological properties of rocks and soils. In: Rubin Y., Hubbard S.S. (eds) Hydrogeophysics. Water Science and Technology Library, vol 50. Springer, Dordrecht. https://doi.org/10.1007/1-4020-3102-5_4

Linde, N. (2014). Falsification and corroboration of conceptual hydrological models using geophysical data. *Wiley Interdisciplinary Reviews: Water*, **1**(2), 151-172. https://doi.org/10.1002/wat2.1011

924 Linde, N., Renard, P., Mukerji, T. and Caers, J. (2015). Geological realism in hydrogeological
925 and geophysical inverse modeling: A review. *Advances in Water Resources*, **86**, 86-101.
926 https://doi.org/10.1016/j.advwatres.2015.09.019

927 Linde, N., & Doetsch, J. (2016). Joint inversion in hydrogeophysics and near-surface
928 geophysics. In: *Integrated imaging of the Earth: Theory and applications*, **218**, 119.
929 https://doi.org/10.1002/9781118929063.ch7

930 Linde, N., Ginsbourger, D., Irving, J., Nobile, F., & Doucet, A. (2017). On uncertainty
931 quantification in hydrogeology and hydrogeophysics. *Advances in Water Resources*, **110**,
932 166-181. https://doi.org/10.1016/j.advwatres.2017.10.014

933 Lu, C., Chen, Y., Zhang, C., & Luo, J. (2013). Steady-state freshwater–seawater mixing zone
934 in stratified coastal aquifers. *Journal of Hydrology*, **505**, 24-34.
935 https://doi.org/10.1016/j.jhydrol.2013.09.017

936 Marshall, S. K., Cook, P. G., Konikow, L. F., Simmons, C. T., & Dogramaci, S. (2020).
937 Conjoint use of hydraulic head and groundwater age data to detect hydrogeologic
938 barriers. *Hydrogeology Journal*, **28**, 1003–1019. https://doi.org/10.1007/s10040-019-
939 02095-9

940 Mesri, G., & Olson, R. E. (1971). Mechanisms controlling the permeability of clays. *Clays and*
941 *Clay Minerals*, **19**(3), 151-158. https://doi.org/10.1346/CCMN.1971.0190303

942 Michael, H. A., & Voss, C. I. (2009). Controls on groundwater flow in the Bengal Basin of
943 India and Bangladesh: regional modeling analysis. *Hydrogeology Journal*, **17**(7), 1561.
944 https://doi.org/10.1007/s10040-008-0429-4

945 Michael, H. A., Scott, K. C., Koneshloo, M., Yu, X., Khan, M. R., & Li, K. (2016). Geologic
946 influence on groundwater salinity drives large seawater circulation through the

947 continental shelf. *Geophysical Research Letters*, **43**(20), 10782-10791.
948 https://doi.org/10.1002/2016GL070863

949 Nguyen, F., Kemna, A., Antonsson, A., Engesgaard, P., Kuras, O., Ogilvy, R., Gisbert, J.,
950 Jorreto, S. and Pulido-Bosch, A. (2009). Characterization of seawater intrusion using 2D
951 electrical imaging, *Near Surface Geophysics*, **7**(5-6), 377–390.
952 https://doi.org/10.3997/1873-0604.2009025

953 Nussbaumer, R., Linde, N., Mariethoz, G., & Holliger, K. (2019). Simulation of fine-scale
954 electrical conductivity fields using resolution-limited tomograms and area-to-point
955 kriging. *Geophysical Journal International*, **218**(2), 1322-1335.
956 https://doi.org/10.1093/gji/ggz185

957 Oldenburg, D.W. & Li, Y. (1999). Estimating depth of investigation in DC resistivity and IP
958 surveys. *Geophysics*, **64**(2), 403-416. https://doi.org/10.1190/1.1444545

959 Palacios, A., Ledo J.J., Linde N., Luquot, L., Bellmunt, F., Folch, A., Marcuello,A., Pilar
960 Queralt, P., Pezard, P.A., Martínez, L., del Val, L., Bosch, D. & Carrera, J (2020). Time-
961 lapse cross-hole electrical resistivity tomography (CHERT) for monitoring seawater
962 intrusion dynamics in a Mediterranean aquifer. *Hydrology and Earth System Sciences*,
963 2020, **24**(4), 2121-2139. https://doi.org/10.5194/hess-24-2121-2020

964 Patchett, J. G. (1975). An investigation of shale conductivity. SPWLA 16th Annual Logging
965 Symposium, 4-7 June, New Orleans, Louisiana. Society of Petrophysicists and Well-Log
966 Analysts.

967 Pool, M., Post, V. E., & Simmons, C. T. (2015). Effects of tidal fluctuations and spatial
968 heterogeneity on mixing and spreading in spatially heterogeneous coastal aquifers. *Water*
969 *Resources Research*, **51**(3), 1570-1585. https://doi.org/10.1002/2014WR016068

970 Power, C., Gerhard, J.I., Tsourlos, P., Giannopoulos, A., (2013). A new coupled model for
971 simulating the mapping of dense nonaqueous phase liquids using electrical resistivity
972 tomography. *Geophysics*, **78**, 1–15. https://doi.org/10.1190/geo2012-0395.1.

973 Qi, Y., El-Kaliouby, H., Revil, A., Ahmed, A. S., Ghorbani, A., & Li, J. (2019). Three-
974 dimensional modeling of frequency-and time-domain electromagnetic methods with
975 induced polarization effects. *Computers & Geosciences*, **124**, 85-92.
976 https://doi.org/10.1016/j.cageo.2018.12.011

977 Revil, A., Cathles III, L. M., Losh, S., & Nunn, J. A. (1998). Electrical conductivity in shaly
978 sands with geophysical applications. *Journal of Geophysical Research: Solid Earth*,
979 **103**(B10), 23925-23936. https://doi.org/10.1029/98JB02125

980 Revil, A., & Cathles Iii, L. M. (1999). Permeability of shaly sands. *Water Resources Research*,
981 **35**(3), 651-662. https://doi.org/10.1029/98WR02700

982 Revil, A., Coperey, A., Shao, Z., Florsch, N., Fabricius, I. L., Deng, Y., Delsman, J.R., Pauw,
983 P.S., Karaoulis, M., de Louw, P.G.B., van Baaren, E.S., Dabekaussen, W., Menkovic, A.
984 & Gunnink, J.L. (2017). Complex conductivity of soils. *Water Resources Research*,
985 **53**(8), 7121-7147. https://doi.org/10.1002/2017WR020655

986 Revil, A., Coperey, A., Deng, Y., Cerepi, A., & Seleznev, N. (2018). Complex conductivity of
987 tight sandstones. Geophysics, **83**(2), E55-E74. https://doi.org/10.1190/geo2017-0096.1

988 Rotzoll, K., Gingerich, S. B., Jenson, J. W., & El-Kadi, A. I. (2013). Estimating hydraulic
989 properties from tidal attenuation in the Northern Guam Lens Aquifer, territory of Guam,
990 USA. *Hydrogeology Journal*, **21**(3), 643-654. https://doi.org/10.1007/s10040-012-0949-
991 9

992 Rücker, C., Günther, T., & Spitzer, K. (2006). Three-dimensional modelling and inversion of
993 dc resistivity data incorporating topography—I. Modelling. *Geophysical Journal*
994 *International*, **166**(2), 495-505. https://doi.org/10.1111/j.1365-246X.2006.03010.x

995 Shalev, E., Lazar, A., Wollman, S., Kington, S., Yechieli, Y., & Gvirtzman, H. (2009). Biased
996 monitoring of fresh water-salt water mixing zone in coastal aquifers. Groundwater, 47(1),
997 49-56. https://doi.org/10.1111/j.1745-6584.2008.00502.x

998 Siena, M., & Riva, M. (2018). Groundwater withdrawal in randomly heterogeneous coastal
999 aquifers. *Hydrology and Earth System Sciences*, **22**(5), 2971-2985.
1000 https://doi.org/10.5194/hess-22-2971-2018

1001 Singha, K., & Moysey, S. (2006). Accounting for spatially variable resolution in electrical
1002 resistivity tomography through field-scale rock-physics relations. Geophysics, **71**(4),
1003 A25-A28. https://doi.org/10.1190/1.2209753

1004 Steklova, K., & Haber, E. (2017). Joint hydrogeophysical inversion: state estimation for
1005 seawater intrusion models in 3D. *Computational Geosciences*, **21**(1), 75-94.
1006 https://doi.org/10.1007/s10596-016-9595-y

1007 Waxman, M. H., & Smits, L. J. M. (1968). Electrical conductivities in oil-bearing shaly sands.
1008 *Society of Petroleum Engineers Journal*, **8**(2), 107-122. https://doi.org/10.2118/1863-A

1009 Werner, A.D., Bakker, M., Post, V.E., Vandenbohede, A., Lu, C., Ataie-Ashtiani, B., Simmons,
1010 C.T & Barry, D. A. (2013). Seawater intrusion processes, investigation and management:
1011 recent advances and future challenges. *Advances in Water Resources*, **51**, 3–26.
1012 https://doi.org/10.1016/j.advwatres.2012.03.004.

1013 Wilkinson, P. B., Meldrum, P. I., Chambers, J. E., Kuras, O., & Ogilvy, R. D. (2006). Improved
1014 strategies for the automatic selection of optimized sets of electrical resistivity

tomography measurement configurations. *Geophysical Journal International*, **167**(3), 1119-1126. https://doi.org/10.1111/j.1365-246X.2006.03196.x

Wilson, S. R., Ingham, M., & McConchie, J. A. (2006). The applicability of earth resistivity methods for saline interface definition. *Journal of Hydrology*, **316**(1-4), 301-312. https://doi.org/10.1016/j.jhydrol.2005.05.004

Xu, S.Z., Duan, B.C. and Zhang, D.H. (2000). Selection of the wavenumber k using an optimization method for the inverse Fourier transform in 2.5D electrical modelling, *Geophysical Prospecting*, **48**(5), 789–796. https://doi.org/10.1046/j.1365-2478.2000.00210.x

Yu, X., & Michael, H. A. (2019). Mechanisms, configuration typology, and vulnerability of pumping-induced seawater intrusion in heterogeneous aquifers. *Advances in Water Resources*, **128**, 117-128. https://doi.org/10.1016/j.advwatres.2019.04.013

Zhou, Q., Bear, J., & Bensabat, J. (2005). Saltwater upconing and decay beneath a well pumping above an interface zone. *Transport in Porous Media*, **61**(3), 337-363. https://doi.org/10.1007/s11242-005-0261-4